Pergamon

Int. J. Heat Mass Transfer. Vol. 39, No. 1, pp. 165–192, 1996

0017-9310/96 $9.50+0.00

0017-9310(95)00095-X

Investigation of flow and heat transfer in corrugated passages—II. Numerical simulations

M. CIOFALO

Dipartimento di Ingegneria Nucleare, Università di Palermo Viale delle Scienze, 90128 Palermo, Italy

and

J. STASIEK and M. W. COLLINS

Thermofluids Engineering Research Centre, City University, Northampton Square, London EC1V 0HB, U.K.

(*Received* 11 *November* 1993 *and in final form* 9 *February* 1995)

Abstract—An experimental and numerical study of flow and heat transfer was conducted for a crossed-corrugated geometry, representative of compact heat exchangers under transitional and weakly turbulent conditions. Three-dimensional numerical predictions were obtained by a finite volume method using a variety of approaches ranging from laminar flow assumptions to standard and low-Reynolds number k–ε turbulence models, direct simulation, and large-eddy simulation. In this paper, the various computational approaches are presented and their relative performance is discussed for various geometries and Reynolds numbers; results are compared with experimental measurements and literature data. Detailed experimental results are presented in Part I.

1. INTRODUCTION

1.1. *Purposes of the present study*

The geometry considered here (Fig. 1) consists of plates which bear sine-wave corrugations and are closely packed at an angle on top of one another. It is completely specified by pitch P and internal height H_i of the corrugations, angle θ, and wall thickness s. A complex flow and temperature field is established in the crossed-corrugated passages, which may result in high wall–fluid heat transfer rates with comparatively low pressure drops.

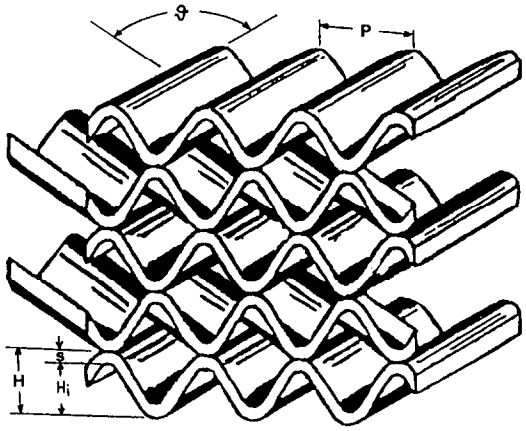

Fig. 1. Cross-corrugated heat transfer elements.

This geometry was selected as representative of various compact heat exchangers, including rotary air pre-heaters for fossil-fuelled power stations [1]. It was made the subject of a comprehensive experimental and predictive research program aimed both at investigating the dependence of overall heat transfer and pressure drop on Reynolds number and geometrical parameters, and at determining the flow patterns in the corrugated passages and the distribution of the local heat transfer coefficient on the heat exchange surface as functions of the geometry and of the operating conditions.

Experimental work involved mainly local Nusselt number measurements by liquid crystal thermography (LCT). Wall pressure distributions were also measured by pressure tappings, and preliminary investigations of the flow field by particle-image velocimetry were conducted. The main results of this study have been documented in a series of confidential reports [2] and are the subject of a companion paper [3].

Here, we concentrate on the parallel numerical simulations relative to $P/H_i = 2$ to 4, $\theta = 30°$ to $150°$, and Reynolds numbers in the range $\sim 10^3$–10^4.

1.2. *Corrugation geometry and performance parameters*

Figure 2 shows a unitary cell of the heat exchange matrix, which was used as the computational domain

NOMENCLATURE

A_c cross-section of unitary cell [m^2]
Δa length of unitary cell [m]
A_μ, A_T, A_{C1}, n, c_0 constants in the low-Re k–ε model, see equation (20)
A^+ constant in Van Driest damping, see equation (22)
c_s Smagorinsky constant, see equation (21)
c_p specific heat [J kg^{-1} K^{-1}]
C_μ, $C_{\varepsilon 1}$, $C_{\varepsilon 2}$, σ_k, σ_ε constants in the k–ε model, see equation(14)
D_{eq} hydraulic diameter, $4S/V$ [m]
f equivalent friction coefficient, see equation (1)
f_w near-wall damping factor, see equation (22)
f_μ, f_1, f_2 terms in the low-Re k–ε model, see equations (15)–(17)
F_i; F_x, F_z ficitious body-force terms, see equation (25) [N m^{-3}]
G mass flow rate in unitary cell [kg s^{-1}]
h convective heat transfer coefficient [W m^{-2} K^{-1}]
H total (external) height of corrugations [m]
H_i internal height of corrugations [m]
i, j, k grid indices along three directions (also as subscripts)
I, J, K number of cells along three directions
j Colburn factor, see equations (29a, b)
k turbulence energy [m^2 s^{-2}]
$\tilde{k}$ subgrid turbulence energy [m^2 s^{-2}]
Nu local Nusselt number, see equation (2)
$\langle Nu \rangle$, Nu_{av} average Nusselt number, see equations (3a,b)
p static pressure [Pa]
$|\Delta p|$ pressure drop in unitary cell [Pa]
P pitch of corrugations [m]; modified pressure, $p+(2/3)\rho k$ or $p+(2/3)\rho\tilde{k}$ [Pa]
Pr Prandtl number
q heat flux [W m^{-2}]
R thermal resistance [K m^2 W^{-1}]
R_T, R_y turbulence Reynolds numbers, see equations (18) and (19)
Re Reynolds number, UD_{eq}/ν
s plate thickness [m]
S surface area of unitary cell [m^2]
S_T fictitious heat sink term, see equation (26) [K s^{-1}]
S_{ij} strain rate tensor, $(\partial u_i/\partial x_j+\partial u_j/\partial x_i)/2$ [s^{-1}]
Sc Schmidt number
Sh Sherwood number
t time [s]
Δt time step [s]
T temperature [K]
U mean velocity [m s^{-1}]
u_i; u, v, w velocity components [m s^{-1}]
u_τ friction velocity, $[(\delta|\Delta p|)/(\rho\Delta a)]^{1/2}$ [m s^{-1}]
V internal volume of unitary cell [m^3]
x_i; x, y, z Cartesian coordinates [m]
y^+ dimensionless distance from wall, yu_τ/ν.

Greek symbols
α thermal diffusivity [m^2 s^{-1}]
β pressure gradient under-relaxation factor, see equation (28)
γ auxiliary angle, $\pi/4$-$\theta/2$
δ conventional channel half-height, $D_{eq}/4$ [m]
Δ mean size of generic grid cell [m]
ε dissipation [m^2 s^{-3}]
θ included angle between corrugations
λ thermal conductivity [W m^{-1} K^{-1}]
ν kinematic viscosity [m^2 s^{-1}]
ξ, η auxiliary coordinates [m]
ρ density [kg m^{-3}]
σ Prandtl number
Φ generic variable
Ψ quadratic invariant of strain rate tensor, $2\,S_{ij}\,S_{ij}$ [s^{-2}].

Subscripts
b thermo-static bath
f fluid (air)
i, j, k directions
s subgrid (unresolved)
t turbulent
w wall.

in the present numerical simulations. The reference frame $Oxyz$ used for the numerical simulations is also reported. Most computational results will be presented for the midplane and the two slices C–C, N–N of the computational domain shown in Fig. 2(b)–(d). The exchanger geometry and the choice of various thermal-hydraulic parameters are discussed in detail in ref. [3]; only short definitions will be given here.

The reference velocity U is defined as $G/(\rho A_c)$, G being the mass flow rate crossing the unitary cell and $A_c = 2PH_i \sin(\theta/2)/\sin\theta$ the cross-sectional area normal to the main flow direction; the Reynolds number Re can be based on this and on the hydraulic diameter D_{eq} (4 × volume/wall surface of the unitary cell).

The pressure drop can be made dimensionless by defining the equivalent friction coefficient:

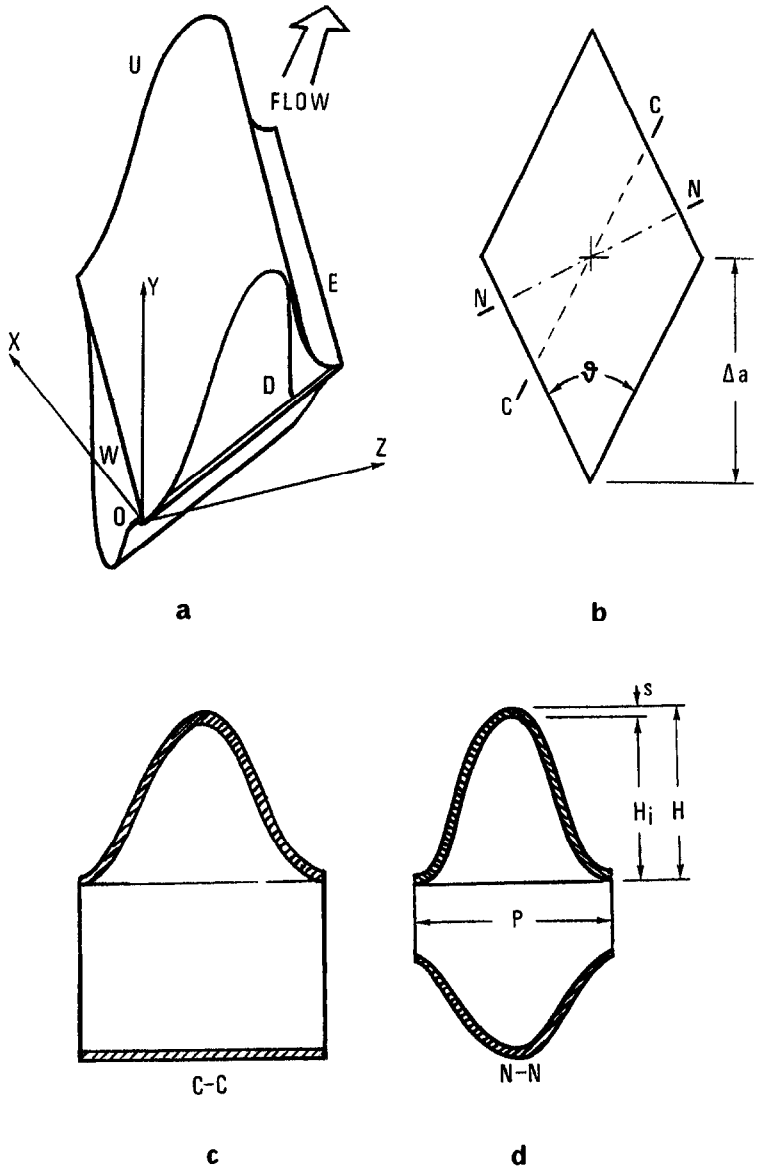

Fig. 2. Unitary cell (computational domain). (a) Perspective view; (b) section with midplane $y = 0$; (c) section C–C parallel to the bottom corrugation; (d) section N–N normal to the top corrugation.

$$f \equiv \frac{|\Delta p| D_{eq}}{\rho \Delta a U^2/2} \tag{1}$$

in which $|\Delta p|$ is the pressure drop between the inlet faces D, W and the outlet faces U, E while Δa is the extent of the unitary cell along the main flow direction, see Fig. 2.

As regards heat transfer, a local Nusselt number can be defined as:

$$Nu \equiv \frac{q_w D_{eq}}{\lambda (T_w - T_f)} \tag{2}$$

in which q_w is the local wall heat flux, T_w is the local wall temperature, T_f is the average (mixing) fluid temperature and λ is the thermal conductivity of the fluid. The mean Nusselt number, which characterizes the overall heat transfer effectiveness of the exchanger, can be defined in two different ways, i.e. either as:

$$\langle Nu \rangle \equiv \frac{1}{S} \int_S Nu \, dS \tag{3a}$$

(S being the lateral surface of a unitary cell), or as:

$$Nu_{av} \equiv \frac{\langle q_w \rangle D_{eq}}{\lambda (\langle T_w \rangle - T_f)} \tag{3b}$$

$\langle q_w \rangle$ and $\langle T_w \rangle$ being the surface-averaged wall heat flux and temperature, respectively. The second definition is more appropriate as an engineering performance parameter. The two definitions coincide for a uniform wall temperature, a condition which is

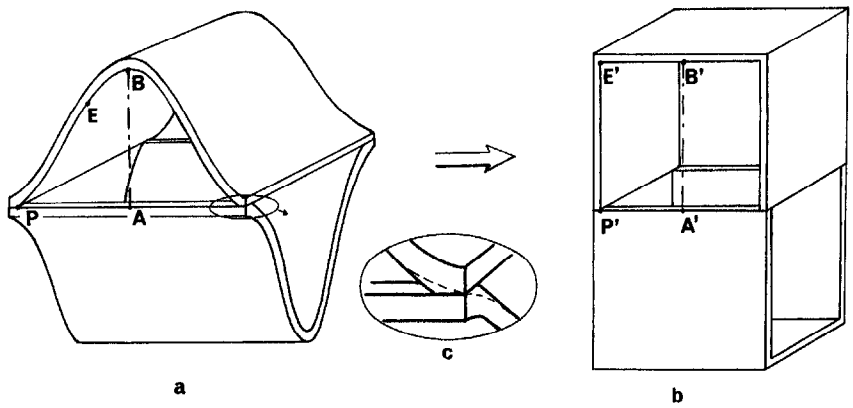

Fig. 3. Smooth mapping of the computational domain onto a cuboid. (a) Computational domain (unitary cell); (b) equivalent cuboid; (c) inset showing replacement of line contact by surface contact at corners.

closely approximated both in real exchangers and in the laboratory tests described here.

Further details of the geometry of the problem and of the various thermohydraulic quantities that can be defined for it are given in ref. [3], which also contains a survey of flow and heat transfer results presented in the literature for this or related configurations. Here we will refer to results presented by Focke *et al.* [4] and Gaiser and Kottke [5], and to our own earlier results presented in refs. [6–8].

2. MODELS AND METHODS

Three-dimensional numerical simulations of fluid flow and heat transfer in the computational domain of Fig. 2 were obtained by the computer code Harwell-FLOW3D, Release 2 [9]. It is based on a finite difference/finite volume technique, allowing for general body-fitted grids [10]. The SIMPLEC pressure–velocity coupling algorithm [11] was used here.

Three basic aspects of the simulations will be discussed in the following, namely: the generation of a computational grid; the treatment of turbulence; and the boundary conditions of the problem. Accuracy considerations and computational aspects will also be mentioned briefly.

2.1. *Computational grid*

The computational domain of Fig. 2 was covered with a three-dimensional array of hexahedral control volumes (i.e. with a 'structured', body-fitted grid) by taking advantage of the fact that it can be mapped smoothly into a cuboid having two inlet and two outlet half-faces (Fig. 3), and is symmetric with respect to a 180° rotation around the main flow direction. In order to avoid singularities in the mapping, the line contact between the upper and the lower plate had to be replaced by a thin surface contact (see inset in Fig. 3); its width was arbitrarily chosen to be equal to the plate thickness s.

A generic control volume of the grid is identified by three indices i, j, k; i increases from one to I going from face D to U of Fig. 2(a), while k increases from one to K going from face W to E. The index j increases from one to J going from the 'trough' of the lower corrugation to the 'crest' of the upper one. For symmetry reasons, $I = K$ here. The grid generation procedure can be summarized as follows.

As a first step, an auxiliary two-dimensional grid was first built in the region PEBA of Fig. 3(a) by generating a regular rectangular grid in the mapped region P′E′B′A′ of Fig. 3(b) and then distorting it as shown in Fig. 4. More precisely, local coordinates ξ and η were introduced in the plane of face D; point E (mapping the corner E′ of the equivalent cube) was arbitrarily located along the tract of sinusoid PB (the choice $\xi_E = (2/3)PA$ was found to be effective); and the final positions of grid points lying on the boundary PEBAP were prescribed by subdividing the two tracts PA and EB (lines j = constant) into N_ξ equal intervals and the two tracts PE and AB (lines k = constant)

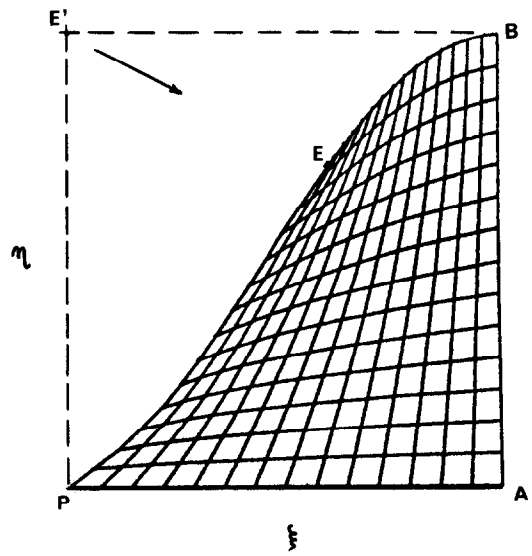

Fig. 4. Generation of an auxiliary two-dimensional grid on an inlet (outlet) face.

into N_η equal intervals. Now, the coordinates of inner grid points were computed by the simple iterative procedure, starting from a uniform rectangular grid in PEBA:

$$\xi_{k,j} = \tfrac{1}{8}(\xi_{k-1,j-1}+\xi_{k,j-1}+\xi_{k+1,j-1}+\xi_{k-1,j}+\xi_{k+1,j}+\xi_{k-1,j+1}+\xi_{k,j+1}+\xi_{k+1,j+1}) \quad (4a)$$

$$\eta_{k,j} = \tfrac{1}{8}(\eta_{k-1,j-1}+\eta_{k,j-1}+\eta_{k+1,j-1}+\eta_{k-1,j}+\eta_{k+1,j}+\eta_{k-1,j+1}+\eta_{k,j+1}+\eta_{k+1,j+1}) \quad (4b)$$

i.e. by computing the grid point coordinates at each iteration as the average of those of the eight neighbours at the previous one. This is basically equivalent to solving a Laplace equation for ξ, η and is similar to the grid-generation method used, for example, by Amsden and Hirt [12]. The method converged quickly to smooth body-fitted grids like that in Fig. 4; typically, consecutive approximations differed by less than one part in 10^5 after ~ 100 iterations. Convergence problems were never observed. Practically identical results were obtained if the four 'diagonal' points were omitted from the summations in equations (4a,b).

Now, additional layers of control volumes in the solid wall, and a final layer of 'dummy' control volumes surrounding the body (used to set boundary conditions in the computational method used), were added by simple algebraic formulae. The explicit resolution of the solid wall is necessary, of course, only if conduction in it is to be taken into account; this was not made in the present simulations, but a single layer of control volumes in the wall was provided for sake of generality.

Finally, the resulting two-dimensional grid was mirror-reflexed, translated and rotated as necessary to span the whole three-dimensional computational domain (unitary cell of the exchanger). Final formulae for the coordinates of grid points (control volume corners) in the reference frame $Oxyz$ of Fig. 2 are:

upper corrugation $y \geqslant 0$ ($i = 1$ to $I+1$, $j = J/2+1$ to $J+1$, $k = 1$ to $K+1$):

$$x_{i,j,k} = \xi_{k,j-J/2}\sin\gamma + \xi_{i,1}\cos\gamma \quad (5a)$$

$$y_{i,j,k} = \eta_{k,j-J/2} \quad (5b)$$

$$z_{i,j,k} = \xi_{k,j-J/2}\cos\gamma + \xi_{i,1}\sin\gamma \quad (5c)$$

lower corrugation $y < 0$ ($i = 1$ to $I+1$, $j = 1$ to $J/2$, $k = 1$ to $K+1$):

$$x_{i,j,k} = \xi_{k,1}\sin\gamma + \xi_{i,J/2+2-j}\cos\gamma \quad (6a)$$

$$y_{i,j,k} = -\eta_{k,j-J/2} \quad (6b)$$

$$z_{i,j,k} = \xi_{k,1}\cos\gamma + \xi_{i,J/2+2-j}\sin\gamma \quad (6c)$$

in which $\gamma = \pi/4 - \theta/2$. An example of the resulting three-dimensional grid is reported in Fig. 5(a) for the case $I = J = K = 32$, $\theta = 45°$, $P/H = 3.66$. The solid (wall) region is evidenced. The only reservation is the strong non-orthogonality of the grid in the regions near the corners (points like E in Figs. 3 and 4); no simple way out of this problem could be found with structured grids, and probably this shortcoming could be eliminated only by recourse to multiblock or unstructured grids (the latter are possible, for example, in the latest release of the same computer code used here).

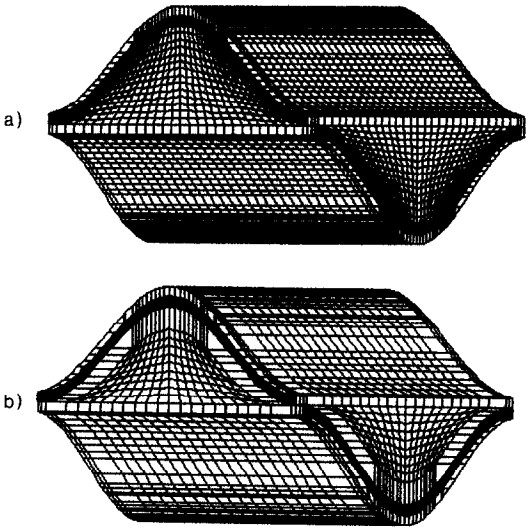

Fig. 5. Three-dimensional grid. (a) Laminar flow, low-Re turbulence model, direct and large-eddy simulation; (b) standard k–ε turbulence model with 'wall functions'.

Grids generated by the above procedure are appropriate either for direct and large-eddy simulations or for conventional, steady-state simulations based on laminar flow assumptions or on a low-Reynolds number turbulence model. However, they are not suitable for simulations using the high-Reynolds number version of the k–ε model in conjunction with the 'wall function' approach. In fact, this treatment requires that the near-wall grid points (control volume centroids) lie well out of the viscous sublayer (say, $y^+ = 11$), while it is easy to show that, for the moderate Reynolds numbers considered here ($Re < 10^4$), the latter covers a significant fraction of the whole computational domain (for example, values of y^+ of about two to three would be obtained for most near-wall centroids using the grid of Fig. 5(a) at $Re \sim 3000$). Thus, when k–ε/'wall-function' simulations were conducted the grid-generation procedure was suitably modified: the wall-adjacent layer of control volumes was generated algebraically so that it had an (approximately) uniform thickness δ, while the iterative algorithm described above was restricted to the inner control volumes. A typical result is shown in Fig. 5(b) for the same corrugation geometry of Fig. 5(a); here, $I = J = K = 24$ and $\delta/H = 0.2$.

2.2. *Governing equations and turbulence modelling*

At the Reynolds numbers considered here (and particularly in the range 1500–3000 which is typical of rotary regenerators) transitional flow is expected. As is well known, such flows are very difficult to simulate by conventional models; for example, even 'low-Reynolds number' turbulence models can predict with some accuracy whether the flow will be laminar or turbulent only for the simplest geometries, and such a capability is probably out of question for the complex geometry studied here.

In order to circumvent—at least partially—this difficulty, predictions were obtained and compared using a variety of modelling approaches, including: (a) laminar flow assumptions; (b) the standard k–ε turbulence model with 'wall functions'; (c) a low-Reynolds number k–ε model; (d) direct simulations; and (e) large-eddy simulations.

In all cases, the continuity, momentum (Navier–Stokes) and temperature equations can be summarized as follows:

$$\frac{\partial u_j}{\partial x_j} = 0 \tag{7}$$

$$\frac{\partial u_i}{\partial t} + \frac{\partial u_i u_j}{\partial x_j} = -\frac{1}{\rho}\frac{\partial P}{\partial x_i} + \frac{\partial}{\partial x_j}[\nu + \nu_t]\frac{\partial u_i}{\partial x_j} + \frac{1}{\rho}F_i \tag{8}$$

$$\frac{\partial T}{\partial t} + \frac{\partial u_j T}{\partial x_j} = \frac{\partial}{\partial x_j}\left[\frac{\nu}{\sigma} + \frac{\nu_t}{\sigma_t}\right]\frac{\partial T}{\partial x_j} + S_T. \tag{9}$$

They are valid for an incompressible, constant-property fluid, are written in 'conservation' form and tensorial notation, and make use of Einstein's convention of implied summation over repeated indices. The terms F_i ($i = 1$ and 3, corresponding to the axes x and z of Fig. 2) are fictitious body forces added only in periodic-flow simulations (see below) in order to account for mean pressure gradients along the corrugations. S_T is a fictitious sink term added for similar purposes to the right-hand side of the energy equation. The various equations undergo appropriate modifications according to the modelling approach used, as discussed below.

Let us consider first conventional, steady-state simulations [models (a)–(c)]. Of course, time derivatives were dropped in equations (7)–(9). Terms containing the turbulent viscosity ν_t were dropped in laminar simulations, while the expression used for ν_t, and the transport equations for k and ε, used in turbulent flow simulations can be summarized both for the standard (high-Reynolds number) k–ε model, and for the low-Reynolds number version used here, as follows:

$$\nu_t = f_\mu C_\mu \frac{k^2}{\varepsilon} \tag{10}$$

$$\frac{\partial u_j k}{\partial x_j} = \frac{\partial}{\partial x_j}\left[\nu + \frac{\nu_t}{\sigma_k}\right]\frac{\partial k}{\partial x_j} + \nu_t \Psi - \varepsilon \tag{11}$$

$$\frac{\partial u_j \varepsilon}{\partial x_j} = \frac{\partial}{\partial x_j}\left[\nu + \frac{\nu_t}{\sigma_\varepsilon}\right]\frac{\partial \varepsilon}{\partial x_j} + C_{\varepsilon 1} f_1 \frac{\varepsilon}{k}\nu_t \Psi - C_{\varepsilon 2} f_2 \frac{\varepsilon^2}{k}. \tag{12}$$

The term Ψ is the quadratic invariant of the strain rate tensor $S_{ij} = (\partial u_i/\partial x_j + \partial u_j/\partial x_i)/2$, proportional to the production of turbulence energy due to shear:

$$\Psi = 2 S_{ij} S_{ij}. \tag{13}$$

The value 0.9 was used for the turbulent Prandtl number σ_t in equation (9). The 'standard' constants C_μ, $C_{\varepsilon 1}$, $C_{\varepsilon 2}$, σ_k and σ_ε were given the 'consensus' values [13]:

$$C_\mu = 0.09 \quad C_{\varepsilon 1} = 1.44 \quad C_{\varepsilon 2} = 1.92$$
$$\sigma_k = 1.00 \quad \sigma_\varepsilon = 1.3. \tag{14}$$

In the standard (high-Reynolds number) version of the turbulence model, $f_\mu = f_1 = f_2 = 1$. On the other hand, in the low-Reynolds number turbulence model used (basically identical to that proposed by Lam and Bremhorst [14]):

$$f_\mu = [1 - \exp(-A_\mu R_y)]^2 (1 + A_T/R_T) \tag{15}$$

$$f_1 = 1 + (A_{C1}/f_\mu)^n \tag{16}$$

$$f_2 = 1 - c_0 \exp(-R_T^2) \tag{17}$$

in which the 'turbulence Reynolds numbers' R_T and R_y are defined as follows:

$$R_T = k^2/(\nu\varepsilon) \tag{18}$$

$$R_y = k^{1/2} y/\nu. \tag{19}$$

Thus, the low-Reynolds number model involves five extra constants A_μ, A_T, A_{C1}, n and c_0 for which the values proposed in ref. [14] were used:

$$A_\mu = 0.0165 \quad A_T = 20.5 \quad A_{C1} = 0.05$$
$$n = 3 \quad c_0 = 1. \tag{20}$$

The above low-Reynolds number turbulence model was chosen because it was found to give good performances for channel flows in a comparison study [15] and was easily implemented in the code [16].

In simulations based either on laminar flow assumptions or on the low-Reynolds number turbulence model ordinary no-slip conditions were used at walls for the momentum equations, and similar conditions (based on a linear flux–temperature relation) for the temperature equation. On the other hand, when the standard k–ε turbulence model was used, linear–logarithmic 'wall functions' were used to 'bridge' the viscous and conductive sublayer; details of these are given by Burns *et al.* [9] and are basically as proposed by Launder and Spalding [13]. Finally, note that in turbulent-flow simulations P includes the static pressure p and the mean normal Reynolds stress, $(2/3)\rho k$.

Actually, laminar simulations were conducted only for $Re \leqslant 5000$, as the assumption of laminar flow

would be unrealistic at higher Reynolds number. For symmetric reasons, standard k–ε/wall function simulations were conducted only for $Re \geqslant 2000$ (however, the requirement that the near-wall grid points lie outside of the viscous sublayer would lead to unacceptably coarse grids for lower Reynolds numbers). Even with these limitations, there is a broad range of Reynolds numbers ($\sim$2000–5000) in which both models were used; as discussed below, the comparison of laminar and turbulent predictions with experimental data was found to be very helpful in understanding transitional phenomena and interpreting the experimental results themselves. Also, in the common range laminar and turbulent predictions provide lower and upper bounds, respectively, for quantities like f and Nu_{av}. The low-Reynolds number turbulence model was used throughout the range $Re = 1000$–10 000, although convergence was found very difficult to attain for $Re \geqslant 4000$ (requiring a large number of iterations and thus of computing time).

In direct and large-eddy turbulent simulations [models (d) and (e)], transient terms in equations (7)–(9) were, of course, retained. In the former case, u_i, P and T were just the instantaneous fields, and additional terms containing ν_t were not present. In large-eddy simulations u_i, P and T must be interpreted as resolved, i.e. large-scale (grid-scale) fields; P is also inclusive of the term $(2/3)\rho\tilde{k}$ ($\tilde{k}$ being the unresolved, or subgrid, turbulence energy). The eddy viscosity ν_t was replaced by the subgrid viscosity, expressed by the Smagorinsky–Lilly model [17, 18]:

$$\nu_s = (c_s f_w \Delta)^2 (2S_{ij}S_{ij})^{1/2}. \tag{21}$$

For the constant c_s the value of 0.08 was used on the basis of previous experience with plane- and ribbed-channel flows [19]. Δ is the average size of the generic grid cell (cubic root of its volume), S_{ij} is the strain rate tensor introduced above and f_w is the Van Driest near-wall damping function [20]:

$$f_w = 1 - \exp(-y^+/A^+) \tag{22}$$

used here with $A^+ = 25$. The eddy heat diffusivity $\alpha_t = \nu_t/\sigma_t$ was replaced by the subgrid heat diffusivity $\alpha_s = \nu_s/\sigma_s$, computed by assuming σ_s (subgrid Prandtl number) = 0.5. Direct simulations were simply obtained by setting $c_s = 0$.

An *a priori* requisite for the direct simulation of turbulent channel flows, suggested for example by Grotzbach [21] on the basis of an analysis by Chapman [22], is that the viscous sublayer $y^+ \leqslant 11$ be resolved by at least three grid points. On the basis of local wall shear stress values from preliminary numerical experiments, it appeared that with a 32^3-volume grid this criterion is just satisfied for $\theta = 37°$ and $Re = 2000$; for larger Re or θ, as the wall shear stress increases and the sublayer becomes thinner, either finer grids or a subgrid model [large-eddy simulation (LES)] should become necessary.

By analogy with plane-channel flows [19], the large-eddy time scale, or LETOT (large-eddy turnover time) was defined as δ/u_τ, where $\delta = D_{eq}/4$ is a 'conventional' channel half-height and $u_\tau = [(\delta|\Delta p|)/(\rho\Delta a)]^{1/2}$ is a 'conventional' friction velocity.

Most simulations were protracted for five LETOTs, using the last two for averaging purposes. Central differencing of advection terms, and Crank–Nicolson time-stepping, were used. The time step Δt was set to 1/50 (LETOT); results obtained using $\Delta t = 1/100$ (LETOT) did not differ significantly.

2.3. *Boundary and initial conditions*

Two different sets of boundary conditions were used on the inlet–outlet faces U,D,E,W of the unitary cell (Fig. 2).

In the first approach, these faces were defined as periodicity surfaces, i.e. surfaces on which the flow variables repeat themselves in a periodic fashion from face D to U and from W to E. In discrete form, this is equivalent to imposing for each flow variable Φ the conditions:

$$\Phi_{1,j,k} = \Phi_{I-1,j,k} \tag{23a}$$

$$\Phi_{2,j,k} = \Phi_{I,j,k} \tag{23b}$$

for D–U periodicity, and:

$$\Phi_{i,j,1} = \Phi_{i,j,K-1} \tag{24a}$$

$$\Phi_{i,j,2} = \Phi_{i,j,K} \tag{24b}$$

for E–W periodicity.

If periodic boundary conditions are imposed, then the intrinsically non-periodic quantities P and T must be replaced by their periodic components (i.e. 'true' P and T plus a term varying linearly along the main flow direction). Pressure losses have to be balanced by including on the right-hand side of the momentum equation (8), for the x and z directions (i.e. $i = 1$ and 3, respectively), the source terms (components of the driving pressure gradient):

$$F_x = F_z = \frac{|\Delta p|}{\sqrt{2}\Delta a}. \tag{25}$$

Similarly heat addition/subtraction to and from the fluid has to be balanced by including on the right-hand side of the energy equation (9) the source/sink term:

$$S_T = \frac{(u+w)}{(\sqrt{2})\Delta a G c_p} \int_s q_w \, dS \tag{26}$$

in which u and w are the (local) velocity components along x and z, respectively, while c_p is the specific heat of the fluid.

This first method is appropriate to simulate the flow and temperature fields in the generic cell of the exchanger, away from intakes (fully developed conditions). The measurement cell in the wind-tunnel test section can be legitimately treated under these assumptions [3].

In the second approach, faces D and W in Fig. 2 were defined as inlets, i.e. surfaces on which the values of all flow variables except pressure were specified (Dirichlet boundary conditions), while the opposite faces U and E were treated as outlets, on which zero-normal derivative (Neumann) conditions were imposed on the same quantities. The heat exchanger matrix of a rotary regenerator, as well as the wind-tunnel test section simulating this, can be considered as composed of identical 'paths' of consecutive cells. For the first (entrance) cell of any path, uniform inlet velocity profiles, aligned with the upper corrugation on face D and with the lower one on face W, were assumed; this seems a reasonable approximation of the actual entry conditions. Sensible values of k and ε, representative of the inlet flow conditions, had also to be assumed in k–ε, turbulent-flow simulations (with both the standard and the low-Reynolds number models). The outlet distributions computed for this cell can now be used as inlet conditions for the next one, and so on.

Within the validity of the approximation of assuming zero-normal derivative conditions on the outlet faces, this method gives the distribution of head losses, heat transfer coefficients, etc. along consecutive cells from the entrance, thus allowing the assessment of entry effects and the simulation of not fully developed situations (as occurred in a previous, smaller test rig). As more and more consecutive cells are considered, results are expected to approach those obtained under periodicity assumptions.

In direct or large-eddy simulations, this latter approach was not tested, as it would have required the complex task of setting an appropriate, time-dependent, inlet flow, and only periodic (fully developed) simulations were conducted.

Hydrodynamic wall boundary conditions were ordinary no-slip for laminar and low-Reynolds number turbulent flow simulations, and standard 'wall functions' for k–ε simulations. Ordinary no-slip conditions were also used in the case of direct simulations, in which the viscous sublayer $y^+ \leqslant 11$ was resolved by at least two or three grid points (they amount to the assumption of a linear relationship between the wall shear stress and the near-wall parallel velocity, as well as between the wall heat flux and the wall-to-cell temperature drop). In large-eddy simulations, however, more general wall boundary conditions were adopted, based on the assumption that universal velocity and temperature profiles hold locally [19]. For near-wall grid points lying within the laminar sublayer these reduce themselves to ordinary no-slip conditions, while for near-wall grid points lying in the turbulent region $y^+ > 11$ they are similar to the 'synthetic' wall boundary conditions adopted for standard k–ε simulations.

As regards thermal boundary conditions, the ones closest to those prevailing in real air heat exchangers are uniform wall temperature conditions, which were thus adopted in most runs. Uniform wall heat flux conditions were also tested, and gave—as expected—slightly larger values of the mean heat transfer coefficients. Finally, in order to draw comparisons of the results with experimental liquid-crystal thermography (LCT) data, a third kind of thermal boundary conditions was used: the bottom wall was assumed to be adiabatic:

$$q_w = 0 \quad \text{(bottom wall)} \tag{27a}$$

while on the opposite wall the following condition was imposed:

$$q_w = (T_b - T_w)/R \quad \text{(top wall)}. \tag{27b}$$

This simulates the conditions holding in the experimental setup, where T_b = constant temperature of the water bath cooling the outer side of the top corrugated plate and R = thermal resistance of the plate + liquid crystal package.

Steady-state periodic simulations were run by imposing the Reynolds number, Re^0 and adjusting the driving pressure gradient $|\Delta p|$ at each SIMPLEC iteration (following a 'settling' phase of about 100 iterations) according to the actual Reynolds number Re, as follows:

$$|\Delta p|^{(\text{new})} = (1-\beta)|\Delta p|^{(\text{old})} + \beta|\Delta p|^{(\text{old})} Re^0/Re \tag{28}$$

β being an under-relaxation factor which was set to 0.9 in most cases. A typical result is shown in Fig. 6 for a periodic laminar flow simulation at $P/H_i = 4$, $\theta = 37°$, $Re^0 = 1000$.

As for the initial conditions, the fastest convergence was generally obtained by simply assuming zero velocity everywhere in the computational domain. In turbulent flow simulations, sensible initial levels of turbulence energy and dissipation had to be set; in most cases, the choice was $k^0 = 0.003\ U^2$, $\varepsilon^0 = 1.5(k^0)^{3/2}/D_{eq}$.

In direct and large-eddy (transient) simulations, in order to avoid the introduction of spurious flow and pressure oscillations, the pressure drop $|\Delta p|$ was imposed, while the flow rate was left free of adjusting itself to a corresponding equilibrium value. A sensible estimate $Re^0 = U^0 D_{eq}/\nu$ was chosen for the initial Reynolds number; initial conditions were set by assuming, in the top and bottom ducts, a plug velocity equal to $U^0/\cos(\theta/2)$ and directed along the corresponding corrugation, and superimposing randomly-generated three-dimensional fluctuations of the order of u_τ. The exact initial fluctuation level was found not to be relevant; also, the fact that the initial flow field was not divergence-free did not constitute a problem for the solution method used here.

2.4. *Further computational details*

All simulations were conducted using the SIMPLEC pressure–velocity coupling algorithm. For steady-state simulations, from 300 to 600 iterations were typically required in inlet–outlet (developing flow) runs, and from 750 to 1200 under periodicity

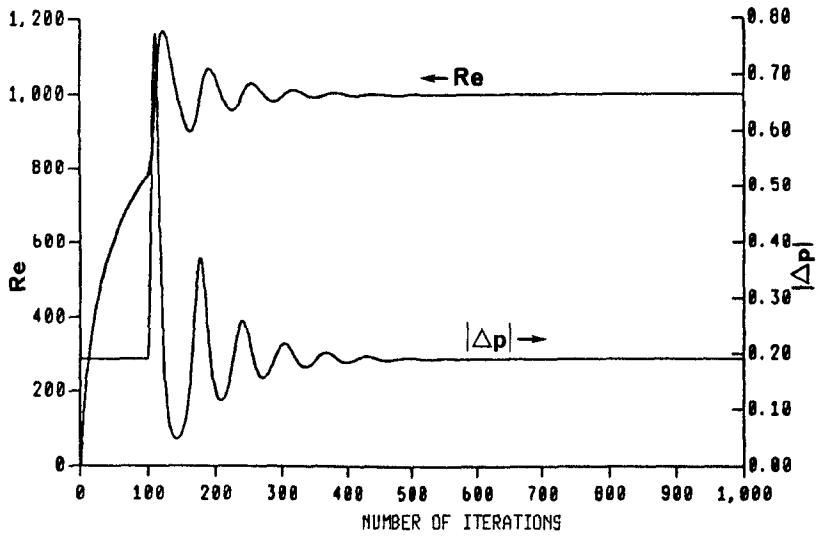

Fig. 6. Behaviour of Re and $|\Delta p|$ in an iterative computation of periodic (fully developed) flow.

(fully developed flow) assumptions, for a satisfactory convergency to be achieved. At the highest Reynolds numbers ($Re > 3000$) small under-relaxation factors (0.2–0.3) had to be used with all models to avoid computational instabilities. With a 32^3-volume computational grid, central processing unit (CPU) times were from 20 to 30 s iteration^{-1} on the IBM 3090-200J of the University of Palermo Computing Centre (used without the Vector Facility option). Thus, typical CPU times were around 8 h for the simulation of fully developed flow under laminar or low-Re turbulent conditions, for each combination of Re, θ and P/H. Since coarser grids (24^3 volumes) were used for k–ε/'wall-function' simulations, CPU times were correspondingly lower (about 10 s iteration^{-1}).

For transient, direct and large-eddy simulations, SIMPLEC was used with just 10 iterations per time step. As discussed above, most simulations were protracted for five LETOTs using 50 time steps per LETOT; thus, a typical run required 2500 overall SIMPLEC iterations. However, due to the better convergence of the linearized equation solvers, the CPU time required per iteration was sensibly less than in steady-state computations, and—using the same 32^3-volume computational grid—overall CPU times were only slightly larger than those required for laminar or low-Re k–ε runs (about 10 h).

On the whole, the CPU time required for the computational part of the present study was well above 1000 h of IBM 3090-200J.

3. RESULTS AND DISCUSSION

3.1. *Pressure drop*

3.1.1. *Fully developed flow.* The behaviour of the equivalent friction coefficient f as a function of the Reynolds number for fully developed (periodic) flow is reported in Fig. 7(a) for $P/H_i = 4$ and $\theta = 37°$. Predictions obtained by using laminar flow assumptions, the standard k–ε method with 'wall functions', the low-Reynolds number turbulence model, and large-eddy simulation, are compared with the experimental data of Stasiek *et al.* [2].

Laminar and standard k–ε computations are unsatisfactory, as they respectively underpredict and overpredict f over most of the Reynolds number range of application. Laminar flow simulations overpredict the Reynolds number dependence of the friction coefficient: they give a Re^{-1} behaviour, while the experimental data exhibit an $Re^{-0.5}$ trend. The best agreement with the experimental data and with their dependence on Re is obtained by using either the low-Reynolds number turbulence model, or LES. Both methods give results which correctly tend to the laminar and to the k–ε ones, respectively, in the limit of very low or very high Reynolds numbers.

The predicted dependence of f on the included angle θ is reported in Fig. 7(b) for $P/H_i = 4$ and $Re = 3000$. As in Fig. 7(a), results from all the computational approaches tested are shown.

Laminar simulations underpredict f over the whole angle range, the severest errors being associated with the largest θ, for which a laminar treatment is obviously inadequate (highly perturbed flow). Standard or low-Re k–ε results exhibit a similar dependence on θ; they both tend to overpredict f slightly at low angles and to underpredict it at high angles. The behaviour of the experimental data suggests transition to turbulence at angles between 37 and 45°. The best prediction of the angle dependence of the friction coefficient is given by LES, which, however, underpredicts f slightly over the whole range of θ.

A comparison of low-Reynolds number k–ε predictions of the friction coefficient with experimental results from the literature is given in Fig. 8 for

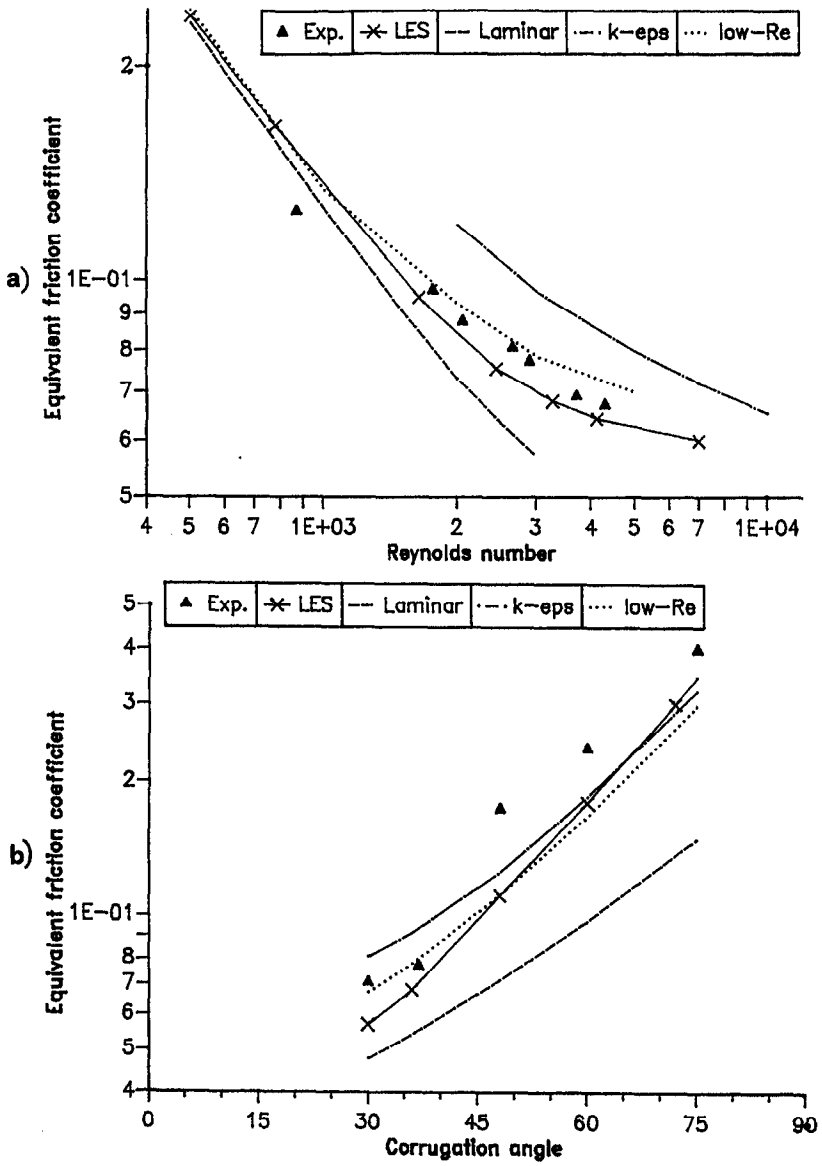

Fig. 7. Predicted vs experimental equivalent friction coefficient for $P/H_i = 4$ (fully developed flow): (a) as a function of the Reynolds number for $\theta = 37°$; (b) as a function of the included angle for $Re = 3000$.

$P/H_i \approx 2$, $Re \approx 2000$ and θ varying between 0 and 180°. Note that for very small or very large included angles the computational domain becomes excessively distorted; therefore, numerical simulations were only conducted for $\theta = 30$–150°. Over this wide range of angles, the overall behaviour of f is predicted fairly well; it should be observed that f increases by more than two orders of magnitude when θ increases from 0 (corrugated ducts parallel to the main flow) to 180° (ducts normal to the main flow). As will be discussed in Section 3.3, some results—in particular those of Focke *et al.* [4]—indicate the presence of a maximum in f for $\theta \approx 150$–160°.

3.1.2. *Developing flow (entry effects).* Entry effects are shown in Fig. 9. The equivalent friction coefficient f predicted by using various modelling approaches is reported as a function of the cell number from the intake for $P/H_i = 3.67$, $Re \approx 3400$ and $\theta = 36°$. The computational method for developing flow is that described in Section 2.3. As mentioned already, predictions for developing flow were not obtained in the case of direct and large-eddy simulation, for which only periodic flow was considered. The geometry is that of the first test section studied in the City University wind tunnel [2]; corresponding experimental values of f for cells 1 and 2, obtained by static wall pressure tappings, are reported in Fig. 9 for comparison purposes. The experimental value for cell 5 is from the similar geometry A described in ref. [3] ($P/H_i = 4$, $\theta = 37°$).

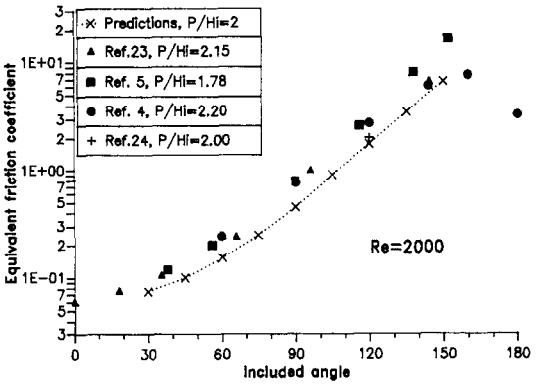

Fig. 8. Comparison between low-Re k–ε predictions of the equivalent friction coefficient and experimental literature results for $P/H_i \approx 2$ and $Re \approx 2000$.

The best predictions of the development of f through consecutive cells are given by the low-Reynolds number turbulence model, which reproduces satisfactorily also the fully developed value of f. Surprisingly, laminar simulations underpredict f but reproduce comparably well its rapid decrease along the first cells. Standard k–ε simulations overpredict only slightly the fully developed friction coefficient, but fail completely to predict entry effects, giving a practically constant value from the first cell on. This shortcoming may have been enhanced by the coarseness of the grid used (24^3 control volumes against the 32^3 adopted for laminar and low-Re k–ε runs).

It should be observed that, in real exchangers, the fluid entering the heat transfer matrix is subjected in the entry region to an abrupt change of direction and cross-sectional area; these effects make the dissipative head loss in the first cells different from the static pressure drop, and thus not adequately described by the friction coefficient defined by equation (1). However, numerical and experimental results suggest that significant entry effects interest only the first few cells, and thus are negligible in large exchangers (rotary air preheaters); they may play a larger role in small regenerative exchangers such as those used in internal combustion engines.

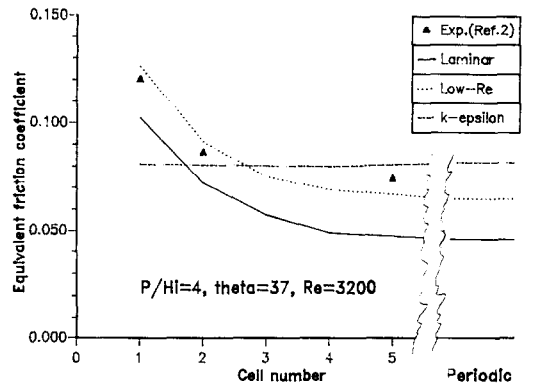

Fig. 9. Friction coefficient in consecutive cells for $P/H_i = 3.67$, $\theta = 36°$ and $Re \approx 3400$. (▲) Experimental results by Stasiek *et al.* [2]; (——) laminar flow; (– – –) standard k–ε model with 'wall functions'; (· · ·) low-Re turbulence model.

3.2. *Heat transfer*

3.2.1. *Fully developed flow.* The average Nusselt number $\langle Nu \rangle$ for fully developed (periodic) flow is reported as a function of the Reynolds number in Fig 10(a) for $P/H_i = 4$ and $\theta = 37°$. As in Fig. 7(a), this includes results from laminar flow assumptions, standard and low-Reynolds number k–ε simulations and large-eddy simulations. Experimental data of Stasiek *et al.* [2], obtained by LCT, are also shown.

As in the case of the friction coefficient, laminar and standard k–ε results are not satisfactory, as they respectively underpredict and overpredict $\langle Nu \rangle$ over most of the range considered. The dependence of $\langle Nu \rangle$ on Re is grossly underpredicted by laminar simulations, which give only a slight increase of $\langle Nu \rangle$ against an experimental trend which can be described by an $\sim 2/3$-power law [3]. Standard k–ε simulations give results only slightly above the experimental data at the highest Reynolds numbers (~ 5000), but overpredict $\langle Nu \rangle$ more seriously at $Re \approx 2000$–3000. For these Reynolds numbers, even with the relatively coarse grid used (see Section 2.1), several grid points lie within the viscous-conductive sublayer and contribute a spurious overprediction of $\langle Nu \rangle$; therefore, k–ε simulations cannot be extended to lower values of Re.

The best agreement with the experiments is obtained again by using the low-Reynolds number turbulence model or LES. Both possess the correct asymptotic behaviour and give results intermediate between laminar and standard k–ε ones. LES results, in particular, reproduce satisfactorily the Reynolds number dependence of the data.

The dependence of $\langle Nu \rangle$ on the included angle θ is shown in Fig. 10(b) for $P/H_i = 4$ and $Re = 3000$. Laminar simulations grossly underpredict $\langle Nu \rangle$ over the whole angle range; the low-Reynolds number k–ε model gives only a moderate underprediction, and LES gives the best results, reproducing the experimental values of $\langle Nu \rangle$ within a few per cent with only a slight overprediction at the smallest angle (30°) and a slight underprediction at the largest (75°). All the above methods, which share the same 32^3-volume computational grid, predict fairly well the angle dependence of $\langle Nu \rangle$; on the other hand, standard k–ε computations, using the coarser 24^3-volume grid, fail to reproduce this and give over the whole range considered an almost uniform average Nusselt number, which crosses transversally the curves relative to the other methods and to the experimental data.

A comparison of predictive and experimental literature values of the average heat/mass transfer coefficients is given in Fig. 11 for $P/H_i \approx 2$, $Re \approx 2000$ and θ varying between 0 and 180°. They are all expressed in the form of an average Colburn j factor, which allows the mass transfer data of Focke *et al.* [4]

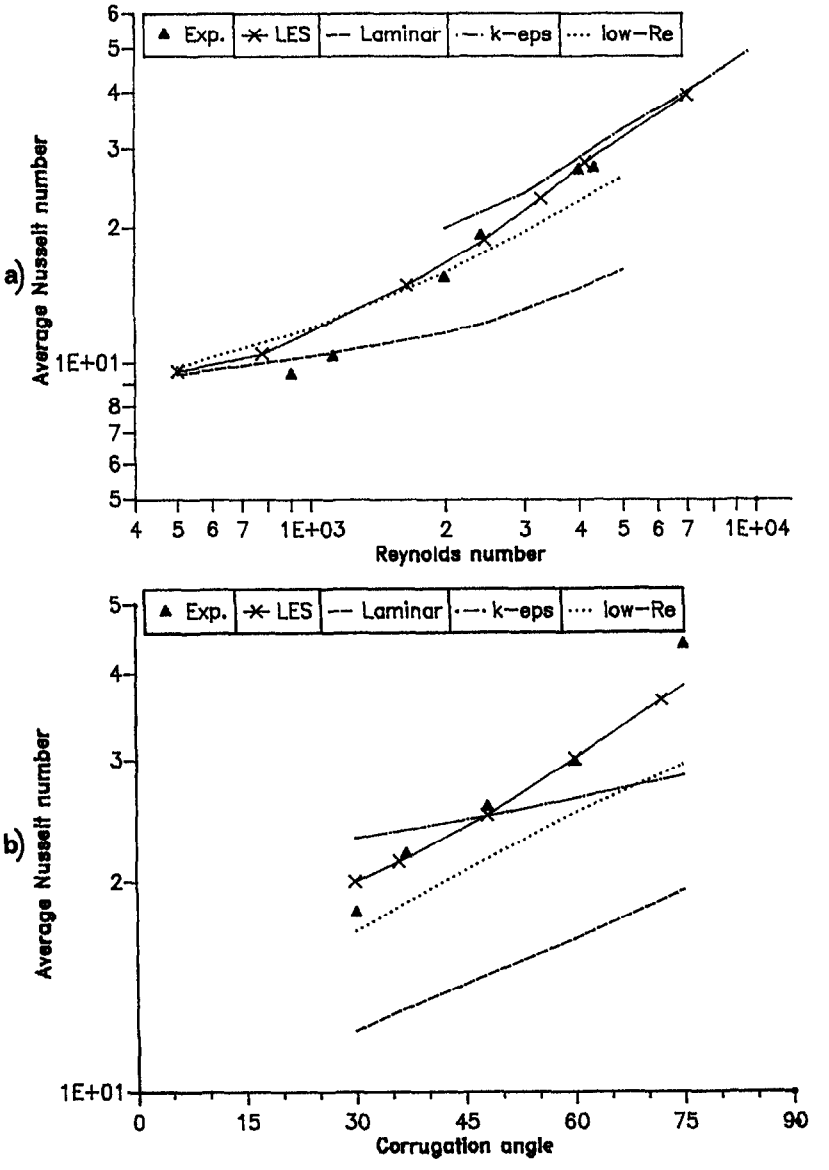

Fig. 10. Predicted vs experimental average Nusselt number for $P/H_1 = 4$ (fully developed flow): (a) as a function of the Reynolds number for $\theta = 37°$; (b) as a function of the included angle for $Re = 3000$.

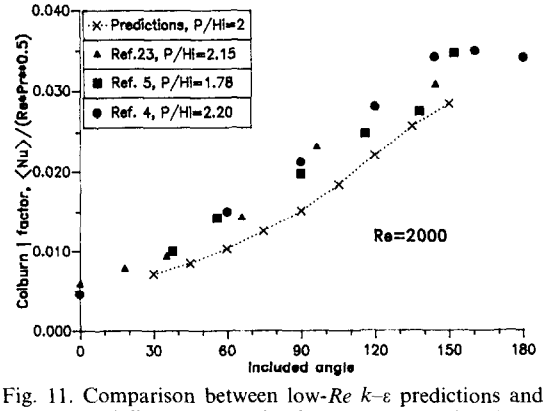

Fig. 11. Comparison between low-Re k–ε predictions and experimental literature results for the average heat/mass transfer coefficient, expressed as Colburn j-factor ($P/H_1 \approx 2$, $Re \approx 2000$).

and Gaiser and Kottke [5] to be included. The j factor is defined as:

$$j = Nu/(Re\,Pr^{0.5}) \quad \text{(heat transfer)} \qquad (29a)$$

$$j = Sh/(Re\,Sc^{0.5}) \quad \text{(mass transfer)} \qquad (29b)$$

Sh and Sc being the Sherwood and Schmidt numbers, respectively (mass-transfer analogues of the Nusselt and Prandtl numbers Nu, Pr). Computational results are all from low-Reynolds number k–ε simulations. Over this wider range of θ, the overall behaviour of $\langle Nu \rangle$ is predicted fairly well; however, an under-prediction by $\sim 20\%$ is obtained for large included angles. It should be observed that $\langle Nu \rangle$ increases by only a factor 3–5 when θ increases from 0 to 180°, i.e. much less than the equivalent friction coefficient in Fig. 8.

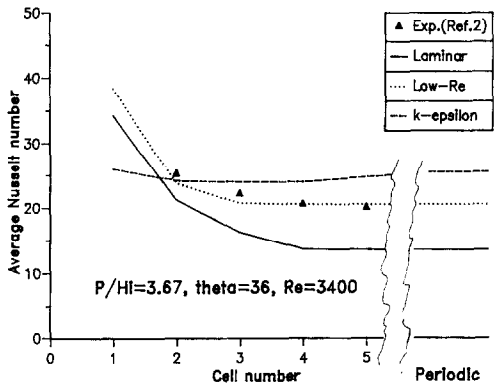

Fig. 12. Nusselt number in consecutive cells for $P/H_1 = 3.67$, $\theta = 36$ and $Re \approx 3400$. (▲) Experimental results by Stasiek *et al.* [2]; (——) laminar flow; (– – –) standard k–ε model with 'wall functions'; (· · ·) low-Re turbulence model.

3.2.2. *Developing flow (entry effects).* Entry effects on the average Nusselt number are shown in Fig. 12. Values of $\langle Nu \rangle$ predicted by using laminar flow assumptions and the standard or low-Reynolds number turbulence models are reported as functions of the cell number from the intake for $P/H_1 = 3.67$, $Re \approx 3400$ and $\theta = 36°$, i.e. for the same geometry and flow rate as in Fig. 9.

Much the same remarks hold as for the friction coefficient in Fig. 9. Significant entry effects, close to those which are experimentally observed, are predicted only by laminar flow simulations or by the low-Reynolds number turbulence model. The latter reproduces better the measured $\langle Nu \rangle$ values both in developing and in fully developed flow (corresponding to cell No. 5 in the experiments). Coarse-grid k–ε/'wall-function' computations fail to reproduce entry effects, though they predict fairly well the fully developed levels of the average Nusselt number.

3.3. *Flow field*

Flow fields in crossed-corrugated passages of the type considered here were studied by Focke and Knibbe [25] using flow-visualization by *o*-cresolphthalein in water (electrode-activated pH indicator). The results are also discussed by Focke *et al.* [4]. These authors concluded that for $0 < \theta < 160°$, apart from side wall reflections, the flow follows mainly the furrows on each plate, Fig. 13(a). The essential feature of the flow for these angles is the two sets of criss-crossing streams which induce secondary swirling motions. The driving force that produces swirl in a furrow is the velocity component of the fluid moving along the opposite duct in a direction perpendicular to the furrow, which is proportional to $U \sin \theta$ and therefore at a maximum for $\theta = 90°$. For larger angles, the interaction between the fluid streams becomes negative, i.e. crossing streams have a retarding effect on each other owing to their dominating velocity components being in opposite directions. As θ increases to $\sim 160°$, presumably due to this retarding effect, a change in flow pattern is observed: the fluid still flows mainly along the furrows, but reflections occur between contact points, yielding zig-zag patterns in parallel, Fig. 13(b). Pressure drop and heat transfer are now at a maximum. For $\theta = 180°$, the phase shift between the plates (which now have their furrows parallel to each other, but normal to the flow) must also be specified. For zero shift, the flow separates on each furrow even for Re as low as 20; the separated flow regions grow in size with increasing Re until they fill the major part of the furrows. Pressure drop and heat transfer rates, however, are slightly lower than for $\theta \approx 160°$. The authors argued that, at intermediate angles, the swirling motions induced by the streams criss-crossing along the furrows are the main determinant in heat or mass transfer.

Indications on the flow structure in arrays of crossed-corrugated ducts also come from the experiments of Gaiser and Kottke [5] which, however, were mainly performed in order to measure local mass transfer coefficients (see Section 3.4 below). These studies confirm that, for included angles below $\sim 140°$, the fluid flows mainly along the furrows of the plates as in Fig. 13(a), while for larger angles it describes a zig-zag pattern and is predominantly aligned with the main flow direction, Fig. 13(b).

The present numerical simulations concentrate mainly on included angles up to 75°, which are those of highest practical interest in heat exchanger applications. Typical comparative fluid flow predictions from all the modelling approaches that have been used are reported in Figs. 14–16 for the case $P/H_1 = 4$, $\theta = 36°$ and $Re \approx 3000$. The main flow direction and the reference velocity U are indicated.

Figure 14 shows the predicted velocity fields in the midplane $y = 0$. Laminar results (a) exhibit a marked concentration of the fluid flow in the central portion of the midplane; two symmetric regions where the fluid turns around the contact points M, N between upper and lower plate are clearly visible, and a wake region downstream of the contact point O is also evident. The k–ε turbulence model (b), probably due also to the coarser grid used, predicts a much flatter velocity distribution, with few significant features. An intermediate behaviour is exhibited by the low-Reynolds number k–ε predictions (c). Finally, time-averaged results from large-eddy simulation (d) look very similar in this plane to laminar predictions, with a marked concentration of the flow in the central region.

Figure 15 reports the predicted in-plane velocity fields for the section C–C in Fig. 2. Laminar results (a) exhibit characteristic parabolic profiles in the lower duct. The k–ε turbulence model (b) gives also for this section very flat profiles, while intermediate results are obtained using the low-Reynolds number model (c). In this plane, time-averaged LES results (d) are very close to the low-Reynolds number turbulent predictions, with velocity profiles less peaked than for laminar flow.

Figure 16 reports the in-plane velocity fields for the cross-section N–N in Fig. 2, normal to the axis of the

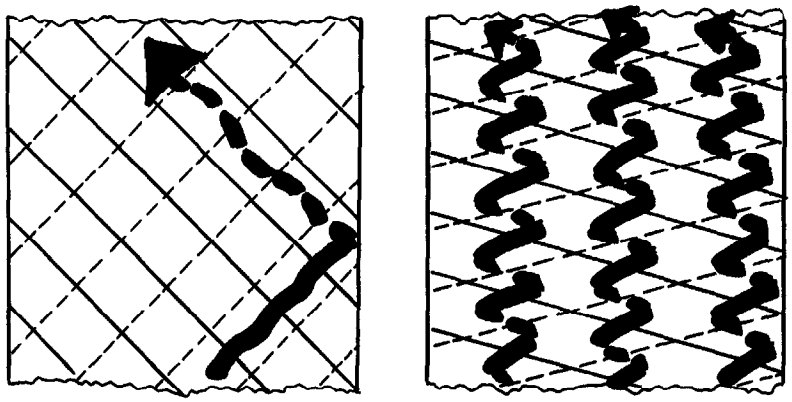

Fig. 13. Flow patterns in crossed-corrugated ducts. (a) Moderate included angle; (b) large included angle.

upper duct. The scale is enhanced in order to evidence the swirling flow patterns, and the (high and uninteresting) velocities in the lower duct are not shown. There are substantial differences between the flow patterns predicted by different modelling approaches. In particular, both the standard and the low-Reynolds number turbulence model (b, c) predict a single vortex, centred roughly on the axis of the duct; laminar and large-eddy simulations (a, d) give results very close to each other and characterized by a more complex secondary flow pattern, with the main vortex shifted downstream along the main flow direction (i.e. to the right in the figures), and a secondary vortex clearly visible in the upstream side of the cross-section (on the left in the figures). The predicted intensity of the swirl, on the other hand, does not change much when different models are used. Further predictions of secondary swirling flow in crossed-corrugated ducts, obtained using either laminar flow assumptions or the standard k–ε model with 'wall functions', were also presented by Henry *et al.* [26].

As mentioned above, Focke *et al.* [4] stressed the importance of swirl in promoting heat (mass) transfer in the present geometry. Unfortunately, detailed velocity measurements are not available to validate the present numerical simulations; some further results obtained by large-eddy simulation are shown in Figs 17–19 in order to illustrate the influence of Re, θ and P/H_1 on the intensity and flow pattern of the swirl.

Figure 17 shows that the relative intensity of the swirl increases markedly with the Reynolds number; the ratio of swirling flow rate to main flow rate increases from ~ 1 to $\sim 5\%$ as Re increases from 780 to 4250. Figure 18 shows that, as the included angle θ increases, both the relative intensity and the complexity of the swirling flow increase; for $\theta = 60°$, as many as four independent vortices develop in the cross-section of the duct. Finally, Fig. 19 compares the swirl patterns predicted for the same Re and θ but for two different values of the pitch to height ratio; as P/H_1 increases, the relative swirling flow rate increases, but secondary vortices disappear and a single recirculation region is established.

3.4. *Distribution of the local heat transfer coefficient*

In order to understand the influence of the geometrical parameters on heat transfer and to design optimized geometries, a knowledge of the distribution of the local heat transfer coefficient is of no less importance than the knowledge of its average value. Figure 20 reports experimental and predicted maps of the local Nusselt number on the top (active) wall of a unitary cell for $P/H_1 = 4$, $\theta = 37°$ and $Re \approx 3900$. The experimental distribution [2] was obtained by LCT and true-colour digital image processing for the fifth cell from the intake of the wind tunnel test section, where fully developed conditions can be assumed to have been attained; numerical results are for periodic flow and thermal fields. The thermal boundary conditions are those described by equations (27a) and (27b), which reproduce closely the experimental conditions; however, very similar results are obtained by setting uniform-wall temperature or uniform-wall flux conditions. Maxima and (local) minima of Nu are indicated by closed triangles and circles, respectively; of course, the absolute minimum of Nu is attained in all cases at the four contact (corner) points.

As discussed in ref. [3], the experimental distribution (a) exhibits a region of intense heat transfer near the downstream end of the right edge of the cell, i.e. in correspondance with impingement on the upper plate by the fluid stream flowing in the lower furrow. Low heat transfer is observed along the upper furrow (almost undisturbed channel flow). Very low heat transfer rates are observed in the stagnation regions surrounding the four contact points between plates.

Clearly, the experimental distribution of Nu is best reproduced by large-eddy simulation (b), which predicts correctly also the values and locations of minimum and maximum, and the average value $\langle Nu \rangle$ (~ 22 for this configuration). Laminar and low-Reynolds number turbulent predictions (c, e) possess the

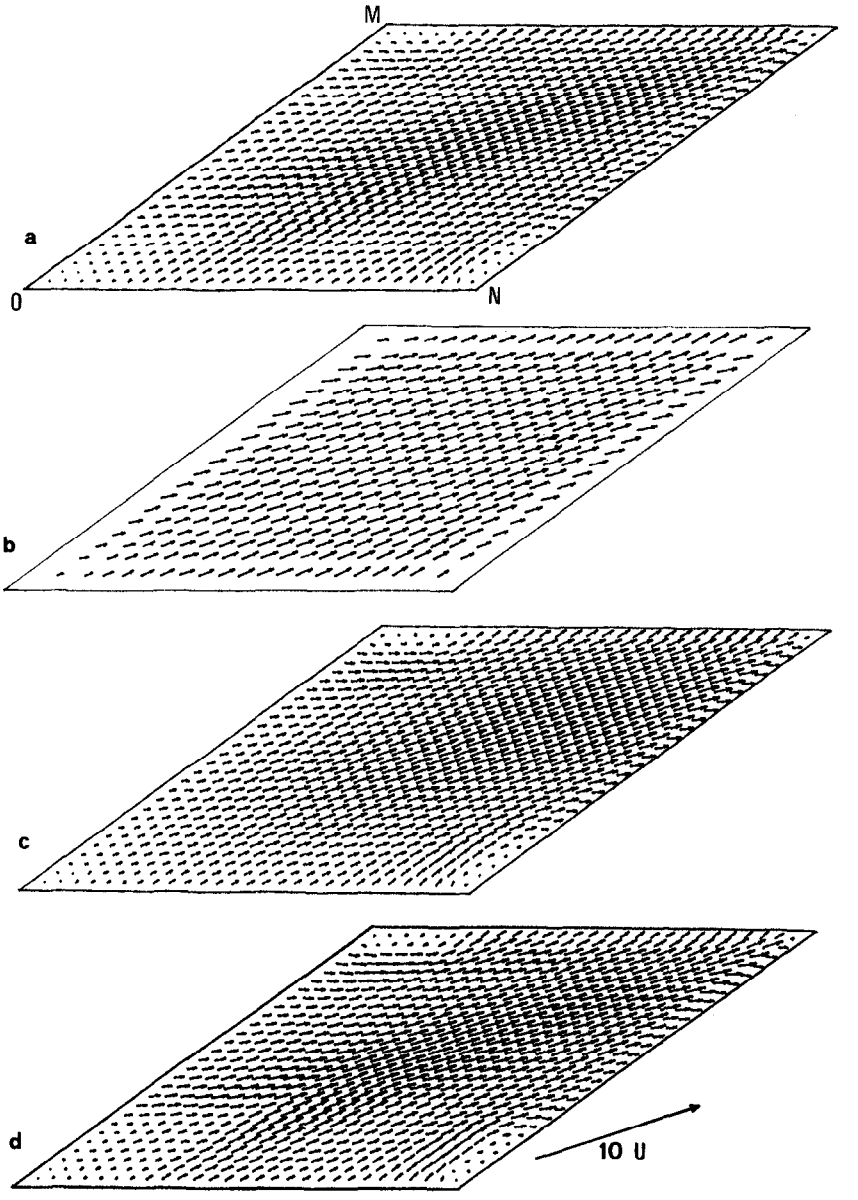

Fig. 14. Predicted velocity fields in the midplane for $P/H_1 = 4$, $\theta = 37^\circ$ and $Re \approx 3000$. (a) Laminar flow; (b) standard k–ε model with 'wall functions'; (c) low-Reynolds number turbulence model; (d) LES (time-averaged).

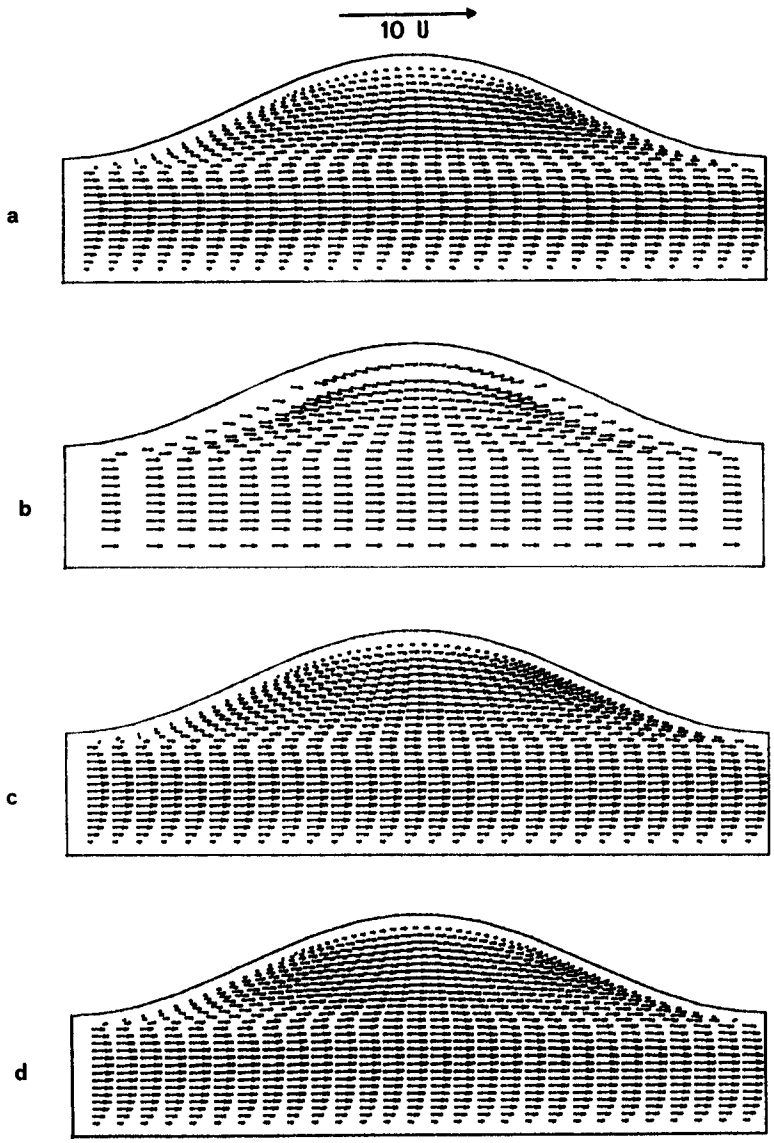

Fig. 15. Predicted velocity fields in the section C–C parallel to the lower furrow for $P/H_1 = 4$, $\theta = 37°$ and $Re \approx 3000$. (a) Laminar flow; (b) standard k–ε model with 'wall functions'; (c) low-Reynolds number turbulence model; (d) LES (time-averaged).

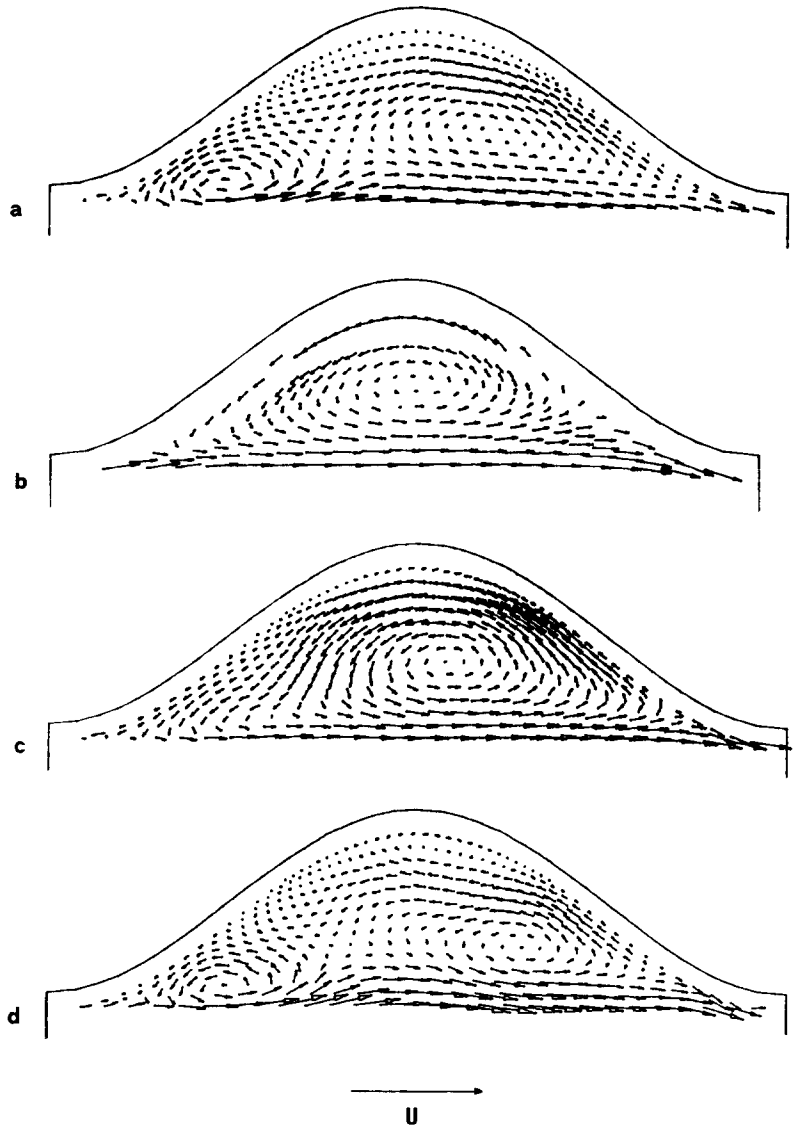

Fig. 16. Predicted velocity fields in the cross-section N–N normal to the upper furrow for $P/H_i = 4$, $\theta = 37^\circ$ and $Re \approx 3000$, showing swirling flow. (a) Laminar flow; (b) standard k–ε model with 'wall functions'; (c) low-Reynolds number turbulence model; (d) LES (time-averaged).

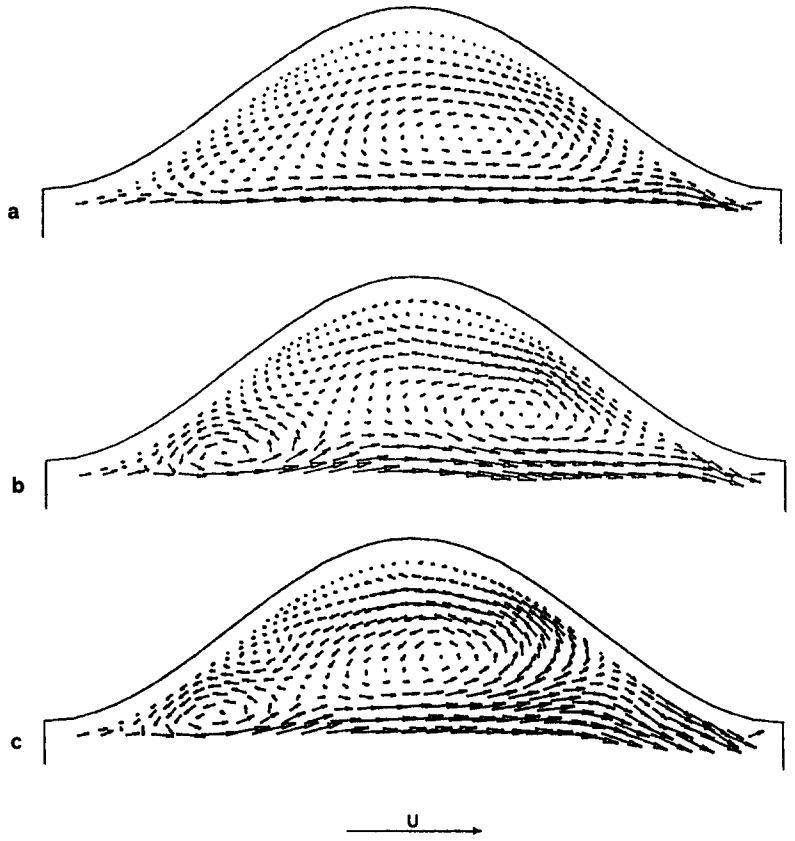

Fig. 17. Swirling flow in the cross-section N–N normal to the upper furrow predicted by LES for $P/H_i = 4$, $\theta = 37°$ and increasing Reynolds number. (a) $Re = 780$; (b) $Re = 2450$; (c) $Re = 4250$.

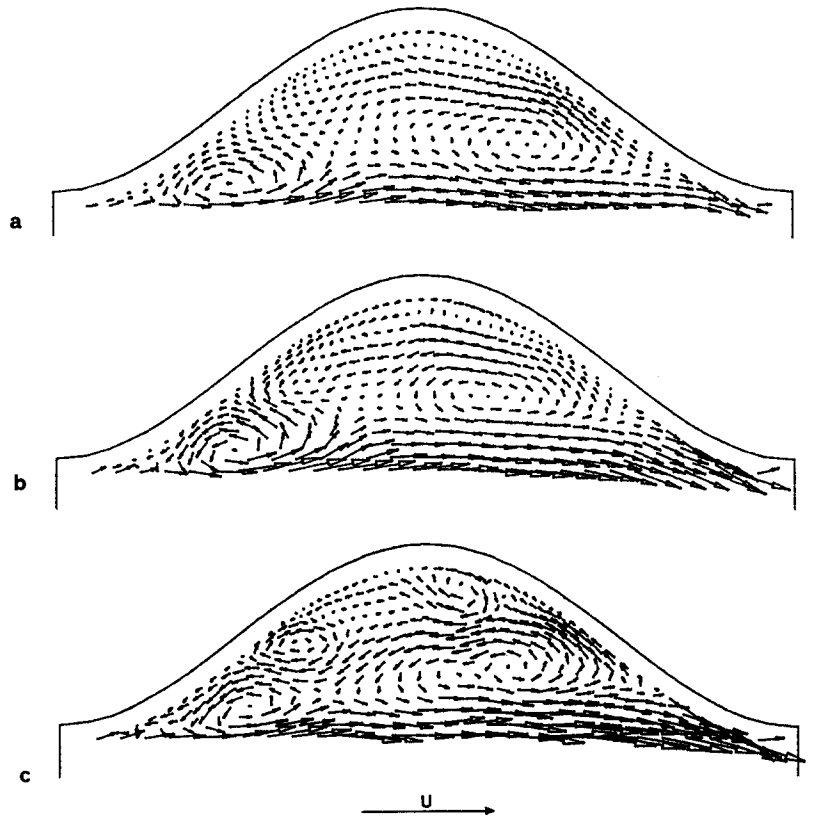

Fig. 18. Swirling flow in the cross-section N–N normal to the upper furrow predicted by LES for $P/H_i = 4$, $Re \approx 2500$ and increasing included angle θ. (a) $\theta = 37°$; (b) $\theta = 48°$; (c) $\theta = 60°$.

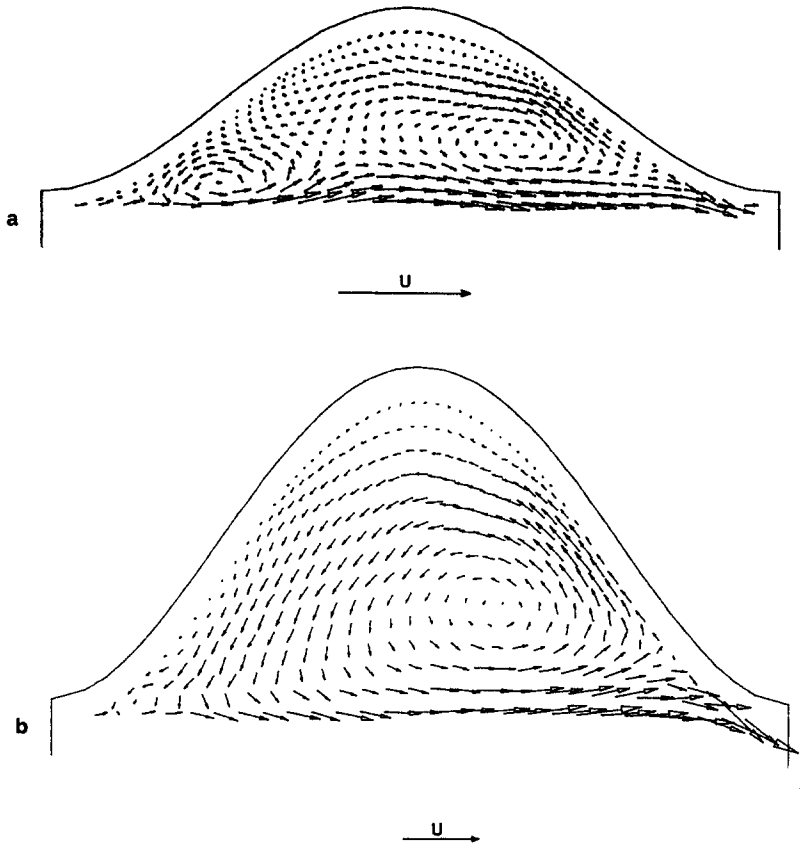

Fig. 19. Swirling flow in the cross-section N–N normal to the upper furrow predicted by LES for $Re \approx 2500$, $\theta = 37^\circ$ and different values of P/H_i. (a) $P/H_i = 4.00$; (b) $P/H_i = 2.22$.

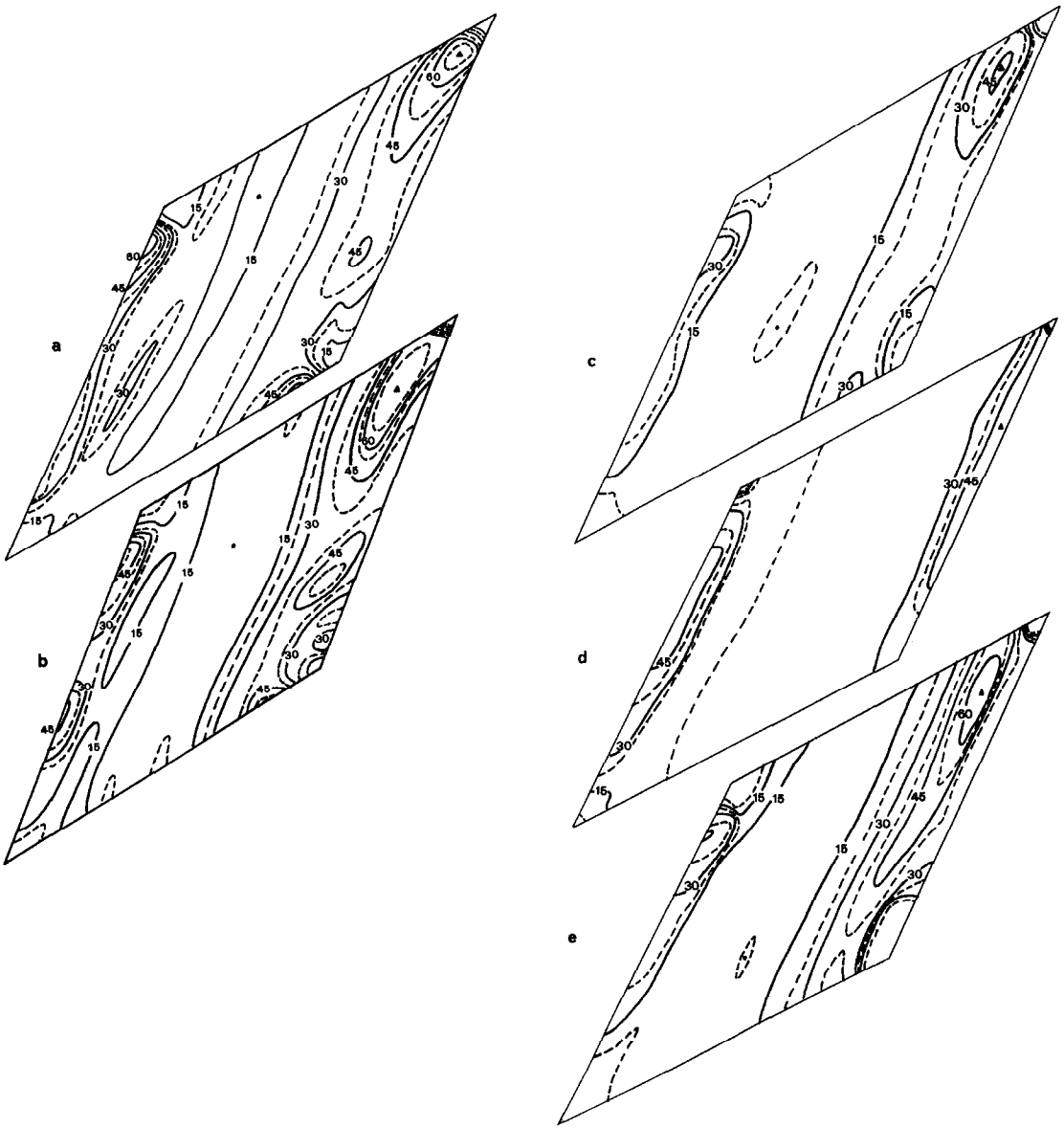

Fig. 20. Distribution of the local Nusselt number on the upper (active) wall of a unitary cell for $P/H_i = 4.00$, $\theta = 37°$ and $Re = 3900$. (a) Experimental measurements by LCT [2]; (b) LES; (c) laminar flow; (d) standard k–ε model; (e) low-Re turbulence model.

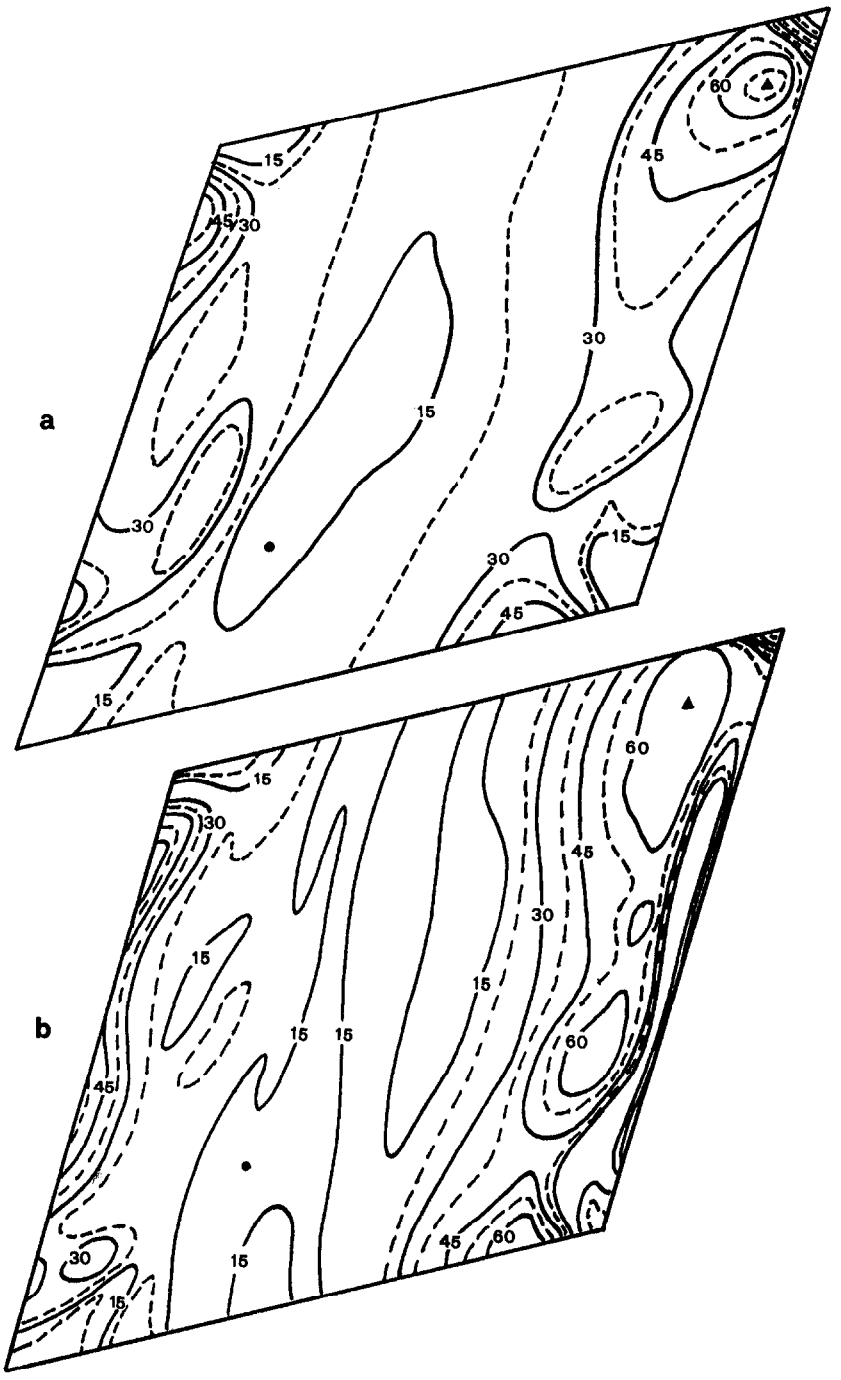

Fig. 21. Distribution of the local Nusselt number on the upper (active) wall of a unitary cell for $P/H_i = 4.00$, $\theta = 60^\circ$ and $Re = 2400$. (a) Experimental measurements by LCT [2]; (b) LES.

same correct qualitative features, differing only quantitatively in the levels of Nu; the better agreement with the experiments is given, as expected, by the latter method. In both cases, the location of the minimum is (wrongly) predicted to be in the upstream portion of the furrow, while the position of the maximum is fairly well computed. The standard k–ε model with 'wall functions' (d) gives a flat distribution of Nu, with few distinctive features; no local minimum is predicted, and the location of the maximum is uncertain (a uniformly high-Nu 'strip' is predicted along the right edge). However, the computed average value of Nu is ~ 23, which differs very little from the experimental and LES result (~ 22).

An additional comparison of experimental and LES distributions of Nu on the top wall of the unitary cell in fully developed flow is given in Fig. 21 for $P/H_i = 4$, $\theta = 60^\circ$ and $Re \approx 2400$. A good agreement is again

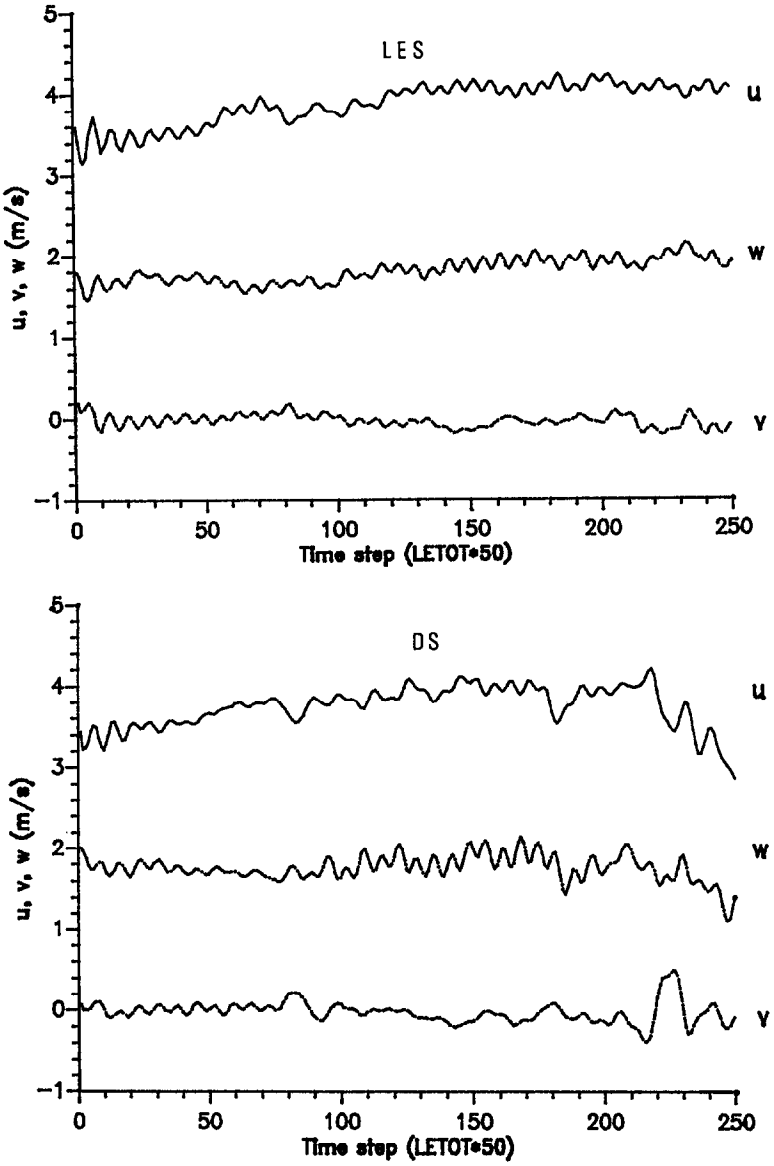

Fig. 22. Behaviour of the three velocity components at a monitoring point (centre of face U in Fig. 2) for $P/H_1 = 4.00$, $\theta = 37°$, $Re \approx 2500$ using LES ($c_s = 0.08$) or direct simulation ($c_s = 0$).

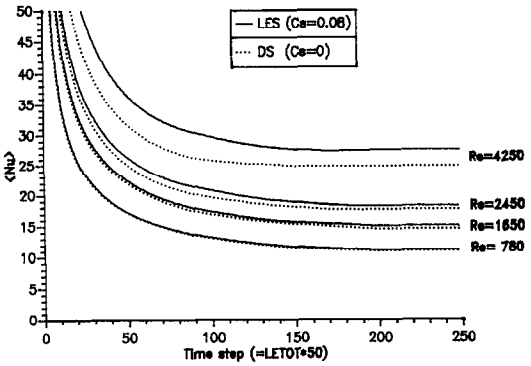

Fig. 23. Behaviour of the average Nusselt number predicted for $P/H_1 = 4.00$, $\theta = 37°$ and increasing Reynolds numbers using a 32^3-volume grid with and without a subgrid model.

observed; note in particular the twin local maxima near the right edge and the location of the minimum in the furrow. For the average Nusselt number, a value of ~ 26 is obtained in this case both from the experiments and from LES.

3.5. *Time-dependent direct simulation/large-eddy simulation results*

Time-dependent results from direct and large-eddy simulations deserve some further discussion, as they elucidate better than steady-state or time-averaged predictions the mechanisms responsible for mixing and heat transfer enhancement.

First, it should be observed that comparative numerical results tend to confirm the *a priori* assessment of direct vs large-eddy simulation discussed in Section 2.2. The behaviour of the three velocity components u, v, w at a monitoring point (centre of the outlet U of the upper duct) is reported in Fig. 22 for the case $\theta = 37°$, $Re \approx 2500$ as computed with a 32^3-volume grid by DS and LES. With a subgrid model, velocities exhibit oscillations of roughly constant amplitude; without, after four LETOTs velocity fluctuations tend to grow excessively.

On the other hand, using the subgrid model at low Re did not produce significant effects. Figure 23 reports the time behaviour of the average Nusselt number predicted by the same grid as above for $\theta = 37°$ and increasing Re with and without a subgrid model; clearly, the subgrid terms do not affect the results significantly for $Re \leqslant 2500$. This shows that, although the Smagorinsky–Lilly model presents the obvious disadvantage of predicting non-zero subgrid diffusivities in laminar flow, for low Reynolds numbers and sufficiently find grids ν_s and α_s are small compared with the molecular diffusivities, and their influence on the flow and thermal fields is negligible.

Note that in all cases, starting from the uniform temperature initial conditions, $\langle Nu \rangle$ decreases for about three LETOTs and attains asymptotic values within five.

When the subgrid model was used, simulations repeated for the reference case with 32^3- and 42^3-volume grids did not show significant differences; coarser grids (e.g. 24^3 volumes) gave markedly different results and exhibited numerical 'wiggles' [19]. Thus, all final simulations were run with the subgrid model and 32^3-volume grids.

The velocity fluctuations in Fig. 22 exhibit a clear dominant frequency F; once made dimensionless as a Strouhal number FT ($T = \Delta a/U$ being the time necessary for the flow to cross the unitary cell), this was found to be about three for all values of Re and θ. Note that u and w are out of phase by about 180°, suggesting that the velocity vector 'swings' (mostly in the horizontal plane) without changing much in amplitude. The physical mechanism yielding these oscillations is clarified by Fig. 24, which compares the time-averaged (a), instantaneous (b) and fluctuating (c) velocity fields in the midplane $y = 0$ for the same case (the reference velocity U is indicated). In the central, 'meandering' region of the midplane, an eddy pattern is clearly superimposed on the mean flow; a detailed examination of instantaneous and fluctuating flow fields shows that the eddies are strongly three-dimensional, though their largest component is vertical. These midplane eddies seem to arise from the instability of the 'spiral' shear layer bounded by the two skewed fluid streams which flow in the upper and lower furrows of the corrugated plates. As expected, their intensity was found to increase both with the Reynolds number (Fig. 25) and with the corrugation angle (Fig. 26), and to be negligible below $Re \approx 1000$ (at least for moderate angles θ).

It should be observed that in LES the main effect of the subgrid model is to build an appreciable subgrid viscosity in this midplane high-shear region; this is shown in Fig. 27 for the same reference case as above. The subgrid viscosity and the associated subgrid thermal diffusivity have the beneficial effect of limiting flow fluctuations while at the same time contributing to cross-stream heat transfer. Note that ν_s does not exceed $\sim 50\%$ of ν, which suggests that an accurate modelling of the subgrid terms is not crucial at the present, low Reynolds numbers.

4. CONCLUSIONS

Numerical predictions were obtained for the flow and thermal fields in a crossed-corrugated geometry under transitional and weakly turbulent conditions, and were compared with well-controlled experimental data. The influence of Reynolds number, included angle and pitch-to-height ratio was investigated, and alternative turbulence modelling approaches were tested.

The standard k–ε model with 'wall functions', while acceptable at high Reynolds numbers and/or included angles, otherwise failed to reproduce the correct values of f and $\langle Nu \rangle$, and gave poor predictions of entry effects and of the local Nusselt number distribution; also, it was completely inapplicable to Reynolds number lower than ~ 2000. On the other hand, simple

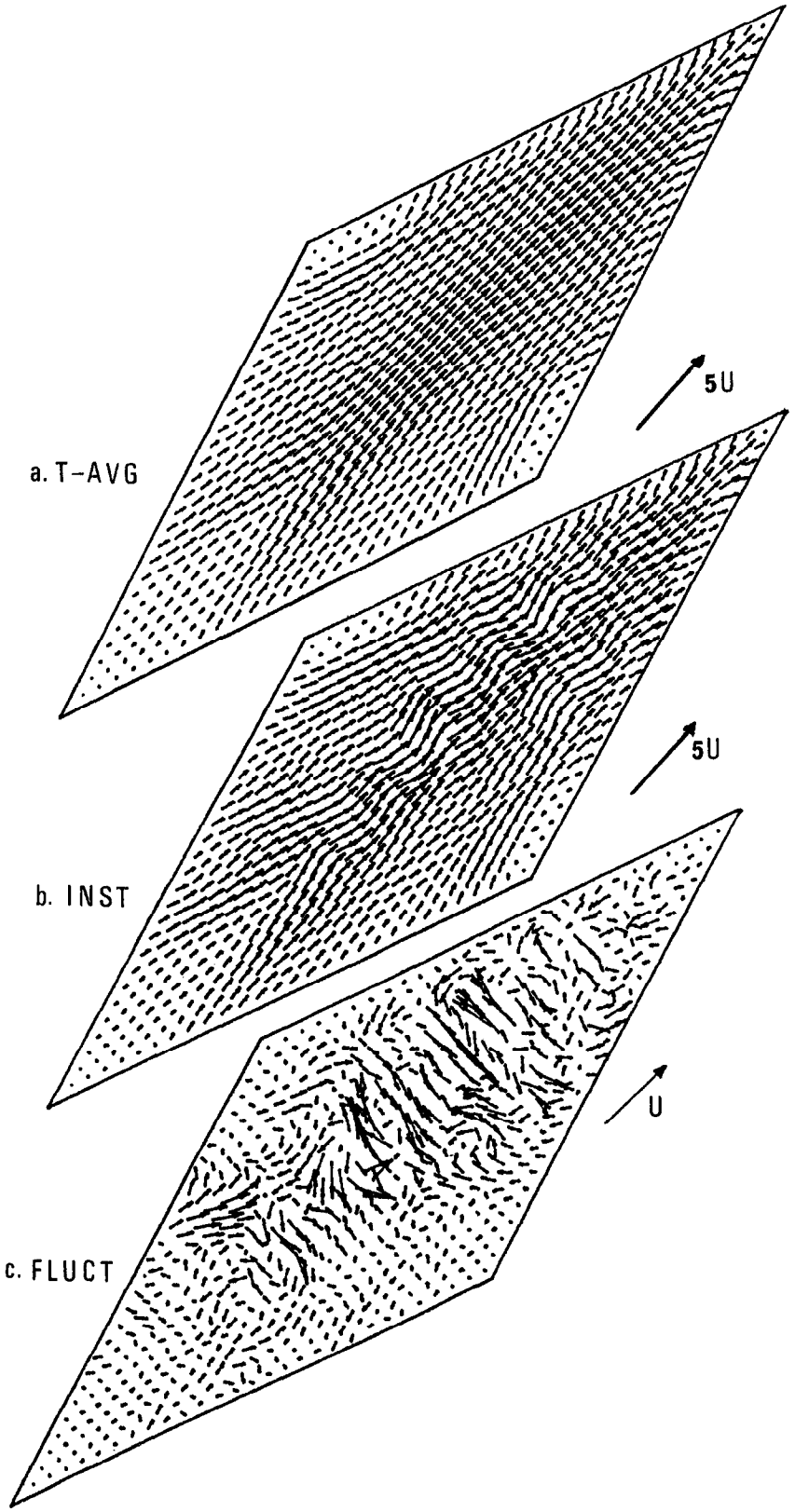

Fig. 24. Midplane velocity fields predicted by LES for $P/H_1 = 4.00$, $\theta = 37°$, $Re = 2450$. (a) Time-averaged over LETOTs 4–5; (b) instantaneous at $t = 4$ LETOTs; (c) fluctuating at $t = 4$ LETOTs [= (b) − (a)].

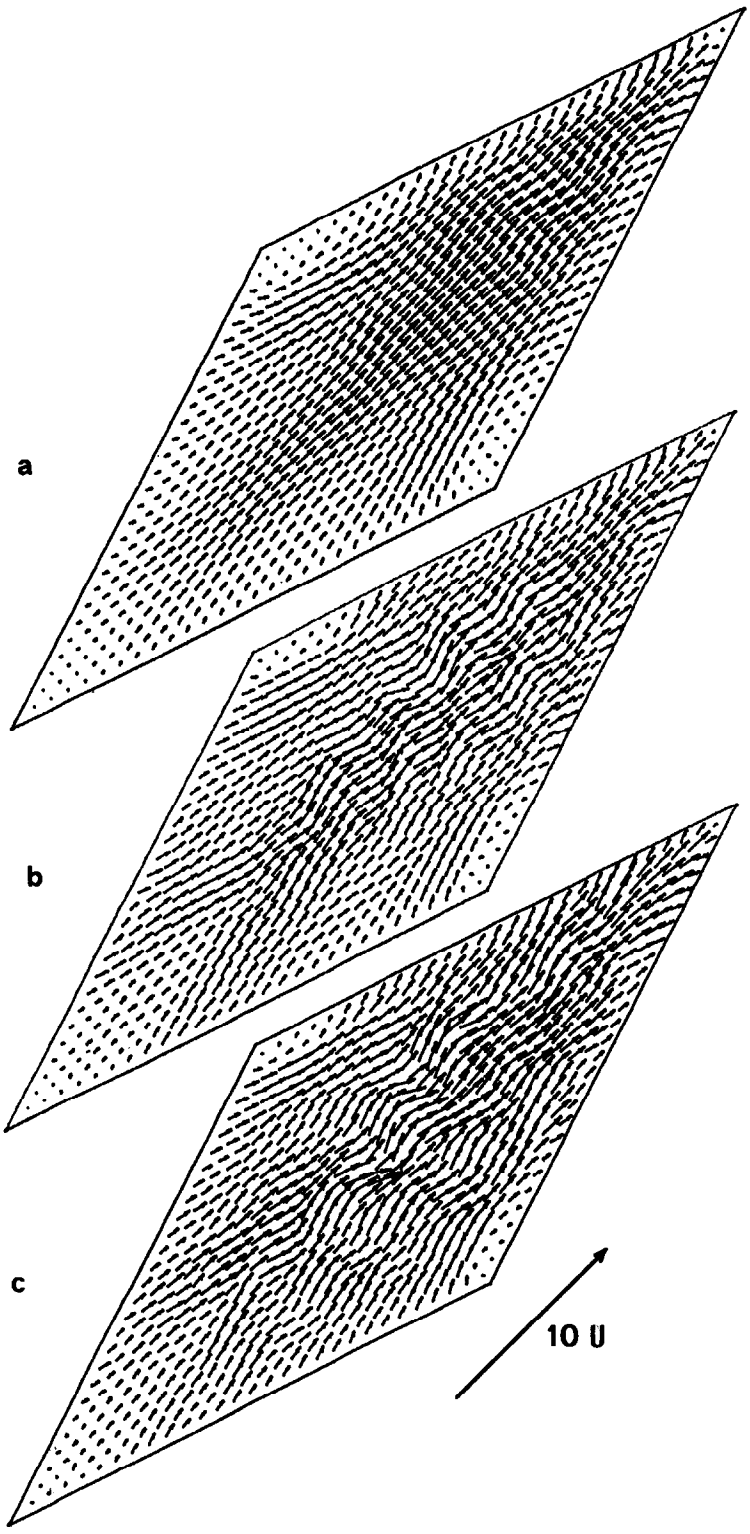

Fig. 25. Instantaneous midplane velocity fields predicted by LES at $t = 4$ LETOTs for $P/H_1 = 4.00$, $\theta = 37°$ and increasing Reynolds number. (a) $Re = 780$; (b) $Re = 2450$; (c) $Re = 4250$.

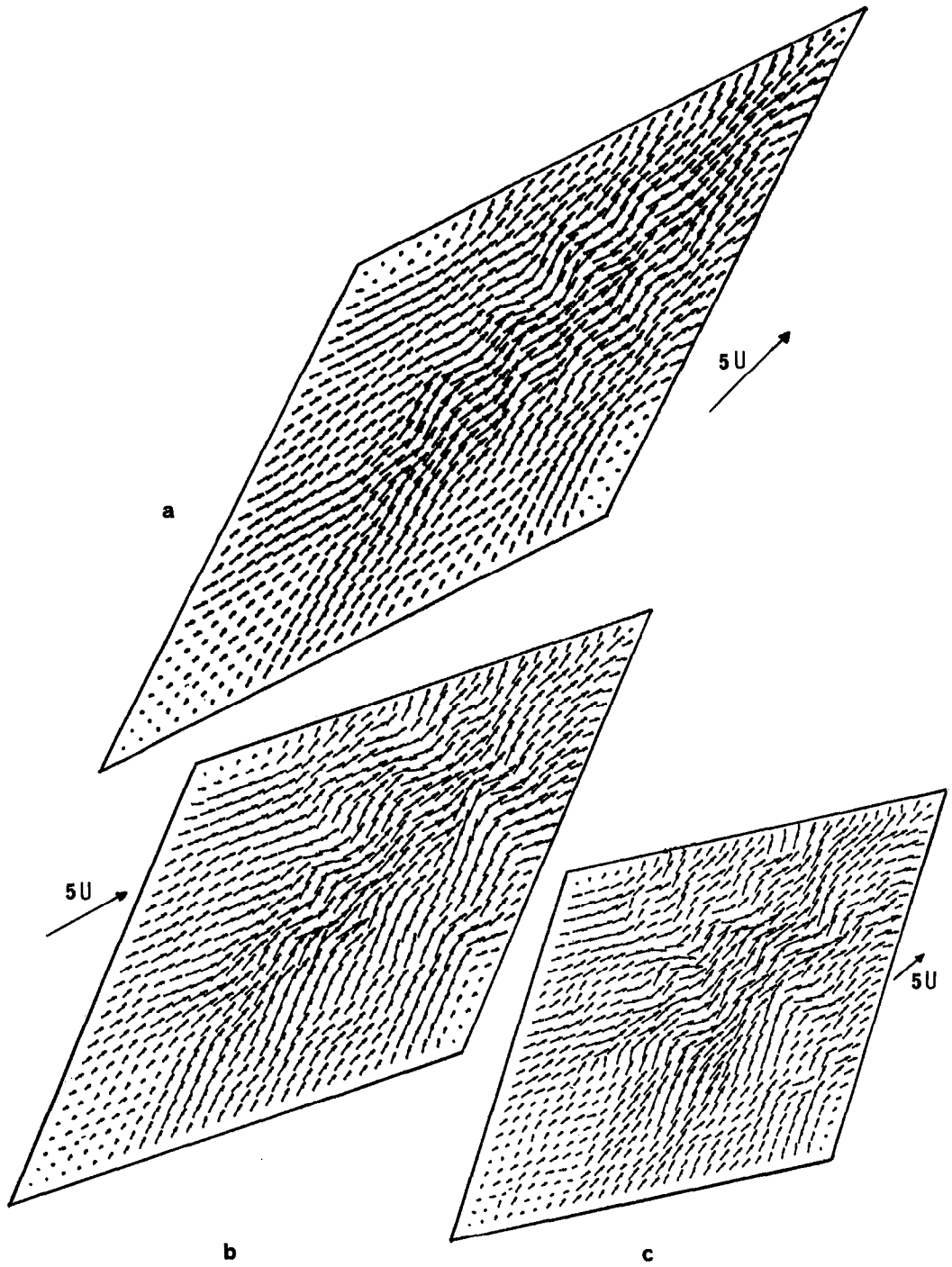

Fig. 26. Instantaneous midplane velocity fields predicted by LES at $t = 4$ LETOTs for $P/H_i = 4.00$, $Re \approx 2500$ and increasing included angle. (a) $\theta = 37°$; (b) $\theta = 48°$; (c) $\theta = 60°$.

laminar flow assumptions yielded acceptable results only for $Re \leqslant \sim 3000$ and moderate angles θ. The best overall agreement with measured friction factors and average or local heat transfer coefficients on the whole range of the parameters was obtained by using either a low-Reynolds number k–ε model or LES. The latter method was only slightly more computationally expensive (for a given grid) than the low-Re model, while providing much more information on the flow behaviour.

A significant swirling flow, induced by the interaction with the fluid flowing in the conjugate duct, was predicted in the cross-section of each furrow. Its (relative) intensity was found to increase with increasing Re, θ and P/H_i; its complexity was found to increase with Re and θ but to decrease with P/H_i.

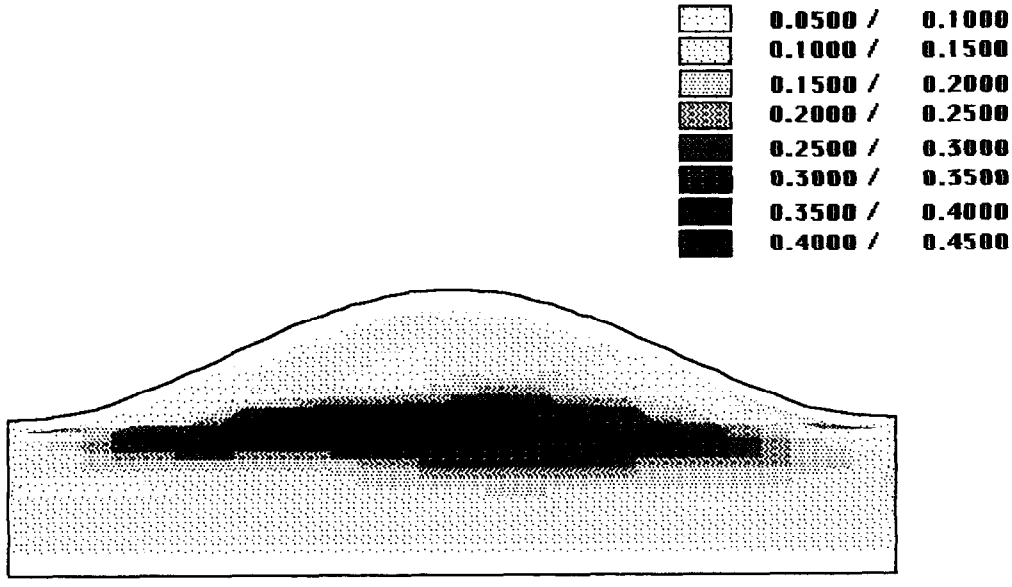

Fig. 27. Time-averaged subgrid viscosity predicted by LES in the plane C–C (parallel to the lower furrow) for $P/H_1 = 4.00$, $\theta = 37^\circ$ and $Re = 2450$.

The swirl intensity was positively correlated with heat transfer rates; this, however, does not necessarily imply a causal effect of swirl on heat transfer enhancement. Experimental data and computational results, particularly from LES, suggest that the principal mechanism responsible for enhanced mixing and heat/mass transfer in this geometry is the instability of the 'spiral' midplane shear layer bounded by the two skewed fluid streams flowing in the upper and lower corrugations. This generates quasi-periodic eddies, particularly intense in the midplane region, which become progressively more intense and irregular as the Reynolds number or the angle θ increase, and contribute significantly to heat transfer. In periodic (fully developed) flow, LES results suggest the existence of a dominating frequency F in the velocity fluctuations which, once normalized by $U/\Delta a$, is ~ 3 in a wide range of Re and θ. The periodic contraction of the cross-section presumably induces a repeated relaminarization, which keeps turbulence levels relatively low. Classic wall turbulence (which would be the dominant heat transfer mechanism in a straight duct) seems to play a secondary role, at least if Re and θ are not too high.

For θ increasing from zero to $\sim 160^\circ$, the equivalent friction coefficient increases by more than two orders of magnitude, while the average Nusselt number increases only by three to five times. At moderate Reynolds numbers and angles θ the crossed-corrugated and similar geometries can give a significant enhancement of heat transfer (as compared with straight ducts) without an undue increase of pressure losses. Of course, this combination of performance is the most desirable for engineering applications.

Acknowledgements—This work was partially supported by PowerGen plc. The authors would like to thank Mr Peter E. Chew (now at Power Technology Centre, Ratcliffe-on-Soar) for many helpful discussions. FLOW3D is a propriety code of AEA Industrial Technology at Harwell. A limited number of the predictive results have appeared in Ciofalo *et al.* [27] at a recent conference of the Institution of Mechanical Engineers.

REFERENCES

1. P. E. Chew, Rotary air preheaters on power station boilers, *Proceedings Symposium on Waste Heat Recovery and Utilisation*. Institute of Energy, U.K. (September 1985).
2. Various authors, Local heat transfer and fluid flow fields in crossed corrugated geometrical elements for rotary heat exchangers, Report Nos. 1–11, Thermofluids Engineering Research Centre, City University, London (October 1989–May 1992); see also A. M. Shand, Particle image velocimetry in a crossed corrugated acrylic section, AEA-EE-0088, Harwell, U.K. (1990).
3. J. Stasiek, M. W. Collins and M. Ciofalo, Investigation of flow and heat transfer in corrugated passages—I. Experimental results, *Int. J. Heat Mass Transfer*.
4. W. W. Focke, J. Zachariades and J. Olivier, The effect of the corrugation inclination angle on the thermohydraulic performances of plate heat exchangers, *Int. J. Heat Mass Transfer* **28**, 1469–1479 (1985).
5. G. Gaiser and V. Kottke, Flow phenomena and local heat and mass transfer in corrugated passages, *Chem. Engng Technol.* **12**, 400–405 (1989).
6. M. Ciofalo, M. W. Collins and F. S. Henry, Laminar and turbulent flow and heat transfer in crossed corrugated heat exchangers. In *Numerical Methods for Thermal Problems* (edited by R. W. Lewis, J. H. Chin and G. M. Homsy), Vol. VIII, Part 1, pp. 622–638. Pineridge Press, Swansea (1991).
7. M. Ciofalo, G. Perrone, J. Stasiek and M. W. Collins, Numerical and experimental study of flow and heat transfer in cross-corrugated rotary regenerators, *Proceedings of the X National Heat Transfer Conference*, pp. 75–86. Unione Italiana di Termofluidodinamica, Italy (1992).
8. M. Ciofalo, J. Stasiek and M. W. Collins, Flow and heat transfer in corrugated passages: direct and large eddy simulation and comparison with experimental results.

In *Engineering Turbulence Modelling and Experiments* 2 (Edited by W. Rodi and F. Martelli), pp. 283–292. Elsevier, Amsterdam (1993).
9. A. D. Burns, I. P. Jones, J. R. Kightley and N. S. Wilkes, Harwell-FLOW3D, Release 2.1: User Manual, AERE-R (Draft), Harwell, U.K. (August 1988).
10. A. D. Burns and N. S. Wilkes, A finite-difference method for the computation of fluid flows in complex three-dimensional geometries, AERE-R 12342, Harwell, U.K. (1987).
11. J. R. VanDoormal and G. D. Raithby, Enhancements of the SIMPLE method for predicting incompressible fluid flows, *Numer. Heat Transfer* **7**, 147–163 (1984).
12. A. A. Amsden and C. W. Hirt, A simple scheme for generating curvilinear grids, *J. Comput. Phys.* **11**, 348–359 (1973).
13. B. E. Launder and D. B. Spalding, The numerical computation of turbulent flows, *Comput. Meth. Appl. Mech. Engng* **3**, 269–289 (1974).
14. C. K. G. Lam and K. A. Bremhorst, Modified form of the k–ε model for predicting wall turbulence, *ASME J. Fluids Engng* **103**, 456–460 (1981).
15. V. C. Patel, W. Rodi and G. Scheuerer, Turbulence models for near-wall and low-Reynolds number flows: a review, *AIAA J.* **23**, 1308–1319 (1985).
16. M. Ciofalo, Implementation of a low-Reynolds number turbulence model for the Harwell-FLOW3D Code (Release 2) and preliminary application to flow and heat transfer problems, TFERC Report (No. 9 of series [2]), City University, London (November 1991).
17. J. Smagorinsky, General circulation experiments with the primitive equations: Part I. The basic experiment, *Mon. Weather Rev.* **91**, 99–164 (1963).
18. D. K. Lilly, On the application of the eddy viscosity concept in the inertial subrange of turbulence, NCAR-123, National Center for Atmospheric Research, Boulder, CO (1966).
19. M. Ciofalo, Large-eddy simulation of turbulent flows with heat transfer in simple and complex geometries, Ph.D. Thesis, Department of Mechanical Engineering and Aeronautics, City University, London (1992).
20. E. R. Van Driest, On turbulent flow near a wall, *J. Aero. Sci.* **23**, 1007 1011 (1956).
21. G. Grotzbach, Direct numerical and large eddy simulation of turbulent channel flows. In *Encyclopedia of Fluid Mechanics* (Edited by N. P. Cheremisinoff), Vol. 6, pp. 1337–1391. Gulf, Houston, TX (1986).
22. D. R. Chapman, Computational aerodynamics development and outlook, *AIAA J.* **17**, 1293–1313 (1979).
23. A. F. Savostin and A. M. Tikhonov, Investigation of the characteristics of plate-type heating surfaces, *Teploenergetika* **17**, 75–78 (1970).
24. K. Okada, M. Ono, T. Tomimara, T. Okuma, H. Konno and S. Ohtani, Design and heat transfer characteristics of new plate heat exchanger, *Heat Transfer—Jap. Res.* **1**, 90–95 (1972).
25. W. W. Focke and P. G. Knibbe, Flow visualization in parallel-plate ducts with corrugated walls, *J. Fluid Mech.* **165**, 73–77 (1986).
26. F. S. Henry, M. W. Collins and M. Ciofalo. Predictions of swirling flow in a corrugated channel, *Proceedings of the Second International Conference on Application of Supercomputers in Engineering* (ASE-91), Boston, MA (1991).
27. M. Ciofalo, M. W. Collins, J. Stasiek and P. E. Chew, CFD and alternative turbulence models applied to heat transfer and pressure drop performance in cross-corrugated heat exchangers, *Proceedings of the conference on Engineering Applications of Computational Fluid Dynamics*, pp. 85–92. Institution of Mechanical Engineers, London (1993).